Nano Today 23 (2018) 73–96

Contents lists available at ScienceDirect

Nano Today

journal homepage: www.elsevier.com/locate/nanotoday

Review

Graphene, related two-dimensional crystals and hybrid systems for printed and wearable electronics

Felice Torrisi*, Tian Carey

Cambridge Graphene Centre, University of Cambridge, Cambridge CB3 0FA, UK

ARTICLE INFO

Article history:
Received 17 July 2018
Received in revised form 9 October 2018
Accepted 29 October 2018
Available online 23 November 2018

Keywords:
Graphene
Two-dimensional materials
Printed electronics
Wearable electronics
Heterostructures

ABSTRACT

Graphene, related two-dimensional crystals and hybrid systems showcase several key properties that can address emerging needs in electronics and optoelectronics, in particular for the ever growing markets of printed, flexible and wearable electronic devices. Graphene's flexibility, large surface area, and chemical stability, combined with its excellent electrical and thermal conductivity, make it promising as a printed flexible electrodes in flexible and wearable electronic devices. Chemically functionalized graphene and self-assembly of graphene-organic molecule composites can also improve mobility and conductivity of organic semiconducting thin film transistors (TFT). Two-dimensional crystals and hybrid systems provide optical and electrical properties complementary to those of graphene, enabling the realization of printed an flexible ultrathin-film photodetectors or photovoltaic systems. Here, we review the use of graphene and related materials for printed and wearable electronics and optoelectronics, defining the roadmap for future applications in this area.

Contents

* Corresponding author.
E-mail address: ft242@cam.ac.uk (F. Torrisi).

https://doi.org/10.1016/j.nantod.2018.10.009

1 Introduction

Ever evolving advances in materials synthesis, solution processing and device design have fueled many of the developments in the field of printed electronics. This technique has progressed from printing text and graphics [1], to a tool for rapid manufacturing [2], being now a well established technique to print TFTs [3–5], light emitting diodes [6,7], photodetectors [8,9], photovoltaic cells [10,11], sensors [12,13] and photonic devices [14,15]. New device integration processes combining flexible and rigid electronic components and the development of scalable roll-to-roll printing processes [15] have resulted in a ever-growing series of electronic and optoelectronic prototypes over the recent years. Following decades of substantial materials development and optimization of printing techniques (including inkjet, flexo, gravure, screen printing or blade, rod, slot-die, spray coating) [11], liquid-dispersed functional materials, such as organic polymers [8,9], nanoparticles [16] and nanotubes [17,18] can now be printed at low temperature (i.e. without causing substrate alterations) and over large areas [11] on either rigid or flexible substrates, and most importantly at a very low cost. By integrating solution-processed electronic materials with high-throughput and additive manufacturing technologies, printed electronics offers a range of attributes and applications complementary to conventional circuits emerging as a reliable platform for heterogeneous integration of various materials.

Application of printed, flexible and wearable components in displays [19,20], high frequency electronics [21], energy harvesting [10,11] and storage, photonics [15] and lighting have fueled the imaginary of new technology platforms for health-care [22,23], aerospace [21], automotive [24], and textile [25] industries [26]. Printable electronic inks are the building blocks of the different parts of a printed device: Semiconducting inks are needed for the active layer, insulating inks for dielectrics, and conducting inks for electrodes. For example, printable conductive inks must be chemically stable (long lifetime, without the need for aggressive post treatments) [27] and highly conductive (>10^4 S/m) [27], while semiconducting inks require high charge carriers mobility (ideally larger than 1 $cm^2 V^{-1} s^{-1}$) and on/off switching ratio (>10^6 for digital applications) [27]. Solution processable nanomaterials are particularly promising in this regard because suitable dispersion engineering can yield liquid-phase inks compatible with printing technologies while maintaining their original unique and desirable electronic, optical and mechanical properties [28]. In particular graphene and other two-dimensional crystals isolated in solution offer a wide source of novel nanomaterials for the creation of a platform of printable inks [29,30] with not only conducting, semiconducting properties but also mechanical strength and chemical stability. For example graphene's near-ballistic transport and high mobility (up to 10^6 $cm^2 V^{-1} s^{-1}$ for a flake by mechanical cleavage) are suitable for electronics [31,32], especially for high frequency applications [33]. Furthermore, its optical and mechanical properties are ideal for photonics [34,35], transparent and conductive composites [36] and electrodes [34], as well as micro and nano sensors [37]. These properties combined with the ease of functionalization [38], and potential for mass production in solution [39,40] makes graphene and excellent platform for printed electronic applications, such as a printed flexible electrode in photodetectors [41] and batteries [42], a transparent conductive electrode for solar cells [43,44] or a printed antenna for ultra high frequency applications [45]. Moreover the bendability of graphene (down to <5 mm bending radius) printed structures [40] has shown marginal effects on the electrical [40] and optical performances [46], opening new opportunities for printed stretchable electronics.

Other two-dimensional (2D) crystals, such as the transition-metal dichalcogenides (TMDs) [47,48] (for example, WS_2, MoS_2, and WSe_2), display insulating, semiconducting (with band gaps in the visible region of the spectrum), and metallic behavior and can enable novel device architectures also in combination with graphene. As for the case of graphene, these materials can be mass-produced in solution and printed on both rigid or flexible substrates demonstrating electronic components such as TFTs and photodetectors as well as novel hybrid structures.

For simplicity, we will refer to graphene, other 2D crystals, and hybrid systems as graphene and related materials (GRMs). The challenge for realistic commercialization of GRM inks for future printed and flexible electronics is to formulate GRM inks by a scalable production process, ensuring reproducibility from batch to batch by following defined standards and scaling factors. Moreover the GRM inks need to be attractive with respect to commercially available materials and products (for example showing better performances at a lower cost or enabling novel functionality creating new printed devices), with tailored electrical, optical and mechanical properties, and printability tunable to several printing techniques. This will require the production of high quality material in high volumes by means of LPE, for example via ultrasonication [49,29,50] or shearmixing [39], or more recently microfluidization [40]. Synthesis of GRM flakes by aggregation of reactive ions or cracking of gas molecules (e.g. graphene production from cracking of methane molecules) can also represent an interesting alternative to LPE GRMs, because of their different morphological, optical and electric properties, and tuning of intentional or unintentional doping from functional groups [51].

Here we review the state of the art of printed and wearable electronics with GRMs. This chapter is organized as follows: Section 1 offers an overview of the electronic inks formulation techniques and their characterisation techniques, in Section 2 we discuss the development of printing strategies for graphene and 2D crystal inks and hybrid combinations, while in Section 3 we overview and discuss the printed electronic and optoelectronic devices with GRMs.

2 Formulation and characterisation of electronic inks

Electronic inks are often mixtures of a functional material, stabilizers and rheology modifiers [52]. Different inks are needed to print the different elements of devices: semiconducting inks (the functional materials) in the active layer, insulating materials for dielectrics, and conducting materials for electrodes. They must be stable, cost-effective and print easily on appropriate substrates to produce devices with high charge-carrier mobility and long lifetime, without the need for aggressive post treatments [52,53]. The functional materials may be GRMs, dispersed nanoparticles (NPs), dissolved organometallic compounds, polymers (both, dissolved and dispersed) or a hybrid mixture of them [52].

The choice of the functional material is mainly determined by the required physical properties of the printed pattern, such as the electrical conductivity, the optical transparency, the mechanical properties (Young's modulus, elongation at break, bending), the adhesion onto the substrate as well as the physicochemical properties of the mixture that composes the ink, such as aggregation and stability, rheology (viscosity, surface tension, density) and by its compatibility with the printing technique (e.g. nozzle size restrictions for nanoparticles when inkjet).

2.1 Ink rheology and surface chemistry

A key property of inks is their ability to be printed or coated. Rheology and surface chemistry describe the liquid flow and solid-liquid interaction, respectively. These are of primary importance to understand and control the ink properties for a specific coating or printing process.

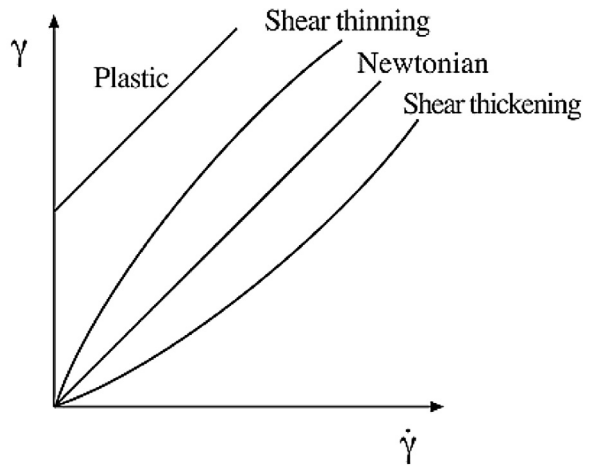

Fig. 1. Different relationships between shear stress and shear rate for Newtonian and non-Newtonian systems leading to Pseudoplastic, Dilatant and plastic behaviour.

Rheology is the study of the physical behavior of all materials when placed under stress [54]. Viscosity (η) is a key rheological property of coatings and inks. This is the resistance of the ink to flow or the ratio of shear stress (τ) to shear rate ($\dot{\gamma}$) (see Eq. (1)). In the case of rotational rheometry, the shear rate (assuming a constant shear rate along the plates for simplicity) considered for a fluid flowing between two parallel plates, one moving at a constant speed and the other one stationary can be described by:

$$\dot{\gamma} = \frac{v}{s} \tag{1}$$

where v is the is the rate of change of displacement (i.e. the velocity of liquid between the two moving plates) and s is the distance between the moving plates. While τ is:

$$\tau = \frac{F}{A} \tag{2}$$

where F is the shear force (tangential to the moving plate) and A is the cross-sectional area of material with area parallel to the applied shear force.

In Newtonian liquids, the $\dot{\gamma}$ varies in direct proportion to the applied τ and η of the liquid can therefore be measured at any $\dot{\gamma}$, giving a true, representative value:

$$\eta = \frac{\tau}{\dot{\gamma}} \tag{3}$$

However, systems like polymer solutions, colloidal solutions, and dispersions often show non-Newtonian behaviour (i.e. a non-linear relation between shear stress and shear rate) and thus a dependance of η on the shear rate. Fig. 1 illustrates the different relationships between shear stress and shear rate for Newtonian and non-Newtonian systems leading to pseudoplastic (shear thinning), dilatant (shear thickening) and plastic behaviour.

The pseudoplastic behaviour is characterised by η decreasing with increasing $\dot{\gamma}$ (typical in polymer solutions, varnishes, glues and resins). Fig. 2 illustrates the pseudoplastic behaviour of two different material systems: dispersion of platelets and polymer chains. At rest the suspension of platelets will have their axe normal to the platelets randomly oriented, while the dispersed polymers arrange following their minimum energy configuration. When shear is applied to the dispersed platelets their normal axis will orient in a direction perpendicular to the shear force, while the polymer backbone will extend in the direction of the shear force. The rearrangement of the platelets in the first case and polymer chains in the second case generates a loss of structural order, moreover the system overcomes Brownian motion between the particulates [55] which results in a reduction of viscosity [56]. Dilatant behaviour consists in η increasing with increasing $\dot{\gamma}$ [56]. Shear thickening behavior occurs when a stable and colloidal suspension of aligned or layered particles transits from an equilibrium state to a state of flocculation (particle aggregation) upon applied shear force. In this case the shear force disrupts the particles order causing a random orientation of the particles and consequent disorder, thus increasing the viscosity in the dispersion [56]. A liquid with plastic or viscoelastic behaviour requires a pre-applied τ before the ink begins to flow. This results in an off-set of the stress strain curve in the τ axes.

Throughout coating and printing processes, mechanical forces of various types are exerted (shear, compressive). The non-Newtonian behaviour for the ink affects the printing operations (in terms of jettability in the case of inkjet, thickness and relative roughness in rod coating, ink transfer in flexographic printing) and requires a tailored rheology for the shear forces exerted while printing. It is thus important to consider viscosities at the $\dot{\gamma}$ required. The pseudoplastic behaviour is considered a desired feature when printing screen or flexographic inks. For example, when printing an ink by screen printing $\dot{\gamma}$ applied by the blade passing onto the orifice of the screen is in the range 50–5000 s^{-1}, this could correspond to an order of magnitude drop in the viscosity of a screen printable ink (static viscosity ~1000 mPa s) [54] with shear thinning behaviour, thus allowing the ink to flow through the screen orifice and "freeze" immediately after once the original viscosity in static condition is restored.

Inks used in flexographic printing typically show a lower viscosity than screen printing inks [57]. However, the effective viscosity of the ink during printing process depends strongly on the shear stress within the printing rollers. From literature, $\dot{\gamma}$ in the range of 1–100 s^{-1} and η between 20 and 500 mPa s are reported as realistic for flexographic printing [57].

Surface chemistry deals with the attractive forces liquid molecules exhibit within each other and with the substrate. All molecules in a liquid are held together by cohesive forces that counteracts the adhesive forces with the air [58].

The cohesive energy, W_c, is the energy required to pull apart a volume of unit cross-sectional area and is given by $W_c = 2\gamma_{LV}$, where γ_{LV} is the surface tension of the liquid in contact with vapour. The adhesive energy, W_a, between a liquid and a solid surface is defined as the reversible work required to separate the unit area of the interface, creating a unit of solid–vapour surface area and a unit of liquid–vapour surface area and is expressed by $W_a = \gamma_{SV} + \gamma_{LV} - \gamma_{SL}$ [59], where γ_{SV} [mJ m^{-2}] is the solid–vapor surface energy and γ_{SL} is the solid–liquid interfacial tension. The cohesive energy between liquid molecules produces the universal property called surface tension γ [mJ m^{-2}]. Surface tension is an essential parameter when designing printable inks and coatings as it determines the jetting and the substrate interaction of the ink [54]. The dynamic surface tension is the change in surface tension before equilibrium conditions are obtained. The time for surface relaxation for a pure liquid is related to the time it takes for the molecules to reach their uniform equilibrium distribution in the liquid. This period is of the order of milliseconds [60].

Considering a liquid droplet stationing on a flat surface (Fig. 3), the contact angle θ_C depends on the liquid surface tension [61–63] and the substrate critical surface tension [61–63], according to the Young's relation [62–64] $\gamma_{SV} - \gamma_{SL} - \gamma_{LV}\cos\theta_C = 0$.

The spreading coefficient, S, is used for predicting whether a liquid drop will spontaneously spread on a solid surface, and is defined as $S = \gamma_{SV} - (\gamma_{SL} + \gamma_{LV})$ [60]. When $S \geq 0$ the spreading process will be spontaneous and result in a thin film, while for $S < 0$ the liquid will form a drop with a contact angle. Changing one or several of these surface energy components makes it possible to control the system to attain the wetting properties desired for a given system.

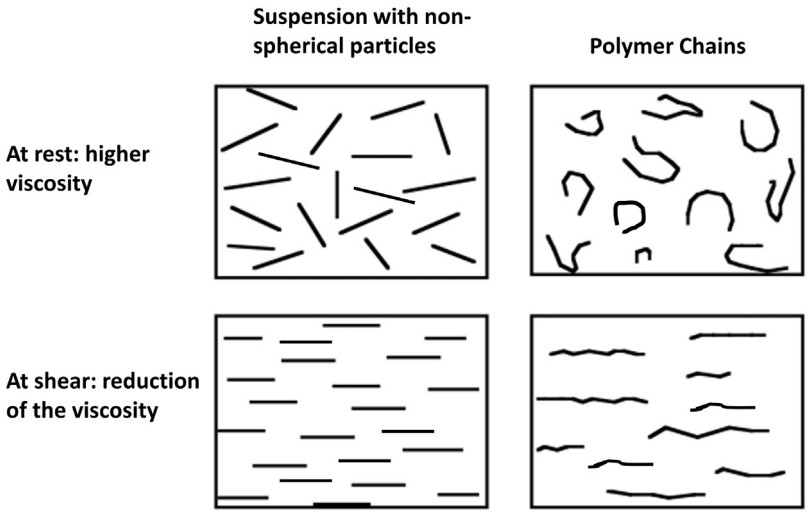

Fig. 2. Pseudoplastic behaviour of two different material systems: dispersion of platelets and polymer chains. Adapted from Ref. [54].

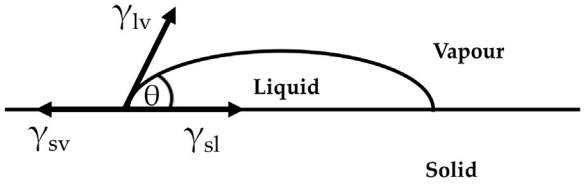

Fig. 3. Schematic of a drop sitting on a rigid substrate where the contact angle is indicated by the three surface tensions (γ_{LV}, γ_{SV}, γ_{SL}).

In flexographic printing the wetting of substrate-liquid determines the ink transfer from the anilox to the substrate and ultimately the printing resolution [11]. Thus tuning of γ_{LV} and γ_{SV} towards maximizing S and W_a while minimizing W_c [62–65] is required. The γ_{LV} for flexographic inks has been reported to vary between 20 and 40 mJ/m^2, hence requiring $\gamma_{SV} > \gamma_{LV}$.

Conversely, a key property of inks viable for ink-jet printing is their ability to generate droplets [66,67]. The jetting of the ink is influenced by η, γ, the density ρ [g cm^{-3}], and nozzle diameter, a [μm] [66]. These can be arranged into dimensionless figures of merit (FOM), such as the Reynolds (Re) [68], Weber (We) [68], and Ohnesorge (Oh) [68] numbers: $\mathrm{Re} = \frac{\upsilon\rho a}{\eta}$; $\mathrm{We} = \frac{\upsilon^2\rho a}{\gamma}$, $\mathrm{Oh} = \frac{\sqrt{We}}{Re} = \frac{\eta}{\sqrt{\gamma\rho a}}$, where υ[m/s] is the drop velocity. During printing, the primary drop may be followed by secondary (satellite) droplets [69–71]. These satellite droplets lead to loss of control over single drop ejection [69–71] and represent an unwanted feature as they decrease the printing definition.

Ref. [72] suggested to use $Z = 1/\mathrm{Oh}$ as the appropriate FOM to characterize drop formation, $Z > 2$ being required to get single drop (i.e. without satellite drop) ejection [72]. The limit $Z > 2$ is obtained from an approximate solution to the Navier–Stokes equations for the case of drop ejection [72]. Later, Ref. [66] reported that in most commercial drop on demand printing systems $1 < Z < 10$ [66], for $Z < 1$ the high viscosity prevents drop ejection [66], whereas at $Z > 10$ the primary drop is accompanied by a number of satellite droplets [66]. More recently, Ref. [71] have experimentally defined $4 < Z < 14$ by considering characteristics such as single drop formability, position accuracy, and maximum allowable jetting frequency. However, different groups have experimentally demonstrated ink-jet printing for $Z > 14$ and $2 < Z < 4$. For example Ref. [73] demonstrated stable printing with $Z = 35.5$ for an Ethylene Glycol(EG)-water ink, while Ref. [69] reported printing with $Z = 68.5$ for glycerol-water ink without satellite drop formation. Also Ref. [1] reported Z from 21 to 91 and no satellite formation for polystyrene nanoparticle inks. Whereas Refs. [74,75] have demonstrated stable printing with Z as low as 2.7 (for glycerol/water ink) and 1 (for photo-resist ink), respectively. However it is generally considered that for an optimum formulation of an ink for ink-jet printing the choice of η, γ and ρ has to target $2 < Z < 14$. The morphological properties (the lateral size in particular for 2D crystals) of the nanoparticles/nanotubes/platelets dispersed in the ink as well as the formation of aggregates in the ink and their accumulation on the print-head can also contribute to printing instabilities. It has been demonstrated [2] that dispersed nanomaterials with lateral sizes smaller than ~1/50 of the nozzle diameter (typically ~400 nm [76,77]) can largely reduce these interfering effects.

2.2 Dispersion of functional layered materials

The functional materials suitable for inks in printed electronics require tailoring to the specific opto-electronic applications (e.g. photovoltaic or light emitting devices, transistors, interconnections) as well as to the mechanical and environmental properties (e.g. degree of mechanical flexibility, temperature or moisture stability) which the devices should be able to perform. For example, the figures of merit (FoM) of interconnections and electrodes for printed electronics are the electrical conductivity and the contact resistance, while FoMs in transparent conductors are optical transmittance (T) and sheet resistance (R_s) [78]. The selected functional materials must be stable, cheap, compatible with appropriate rheology, show long shelf life, without the need for aggressive post-treatments. Graphite and layered crystals can be exfoliated in a large number of two-dimensional nanosheets by LPE [49,29], high-shear mixing [39] and microfluidic exfoliation [40]. While graphite is the most well-known layered crystal, numerous others exist such as hexagonal boron nitride (h-BN) [79], transition metal dichalcogenides (TMDs) [80], oxides [80,81], III-VI semiconductors [80], MXenes [82], layered silicate minerals [83], or layered double hydroxides (LDHs) [84]. These possess different intrinsic properties; for example, while BN is an insulator, graphene is a conductor and TMDs are mostly semiconductors with bandgaps ranging from less than 1 eV to ~2 eV, representing the elemental building blocks of future electronics and optoelectronics. These liquid-dispersed nanosheets are an ideal play-ground for chemical modification [85], composite formation by solution mixing [36,86,87] as well as the production of films or coatings by methods such as inkjet printing [88,89,41] and screen printing [90,91], drop casting [92] and dip

casting [93], and spin coating [94,43] and spray coating [95], thus representing an ideal platform for printed electronics and optoelectronics.

Exfoliation in liquids can be mainly classified in the two main categories of intercalation-based exfoliation and LPE. Intercalation-based methods have long been used to widen the interlayer gap of layered crystals leading to the creation of intercalation compounds [85,96], which can be exfoliated in liquids to give few-layer nanosheets. However, reductive chemical intercalation often requires the use of inert gas conditions and harsh chemical treatments, which can result in the introduction of defects [97,98].

Moreover, the intercalation process normally generates negatively charged flakes with properties distinct from the neutral counterparts. In the case of graphene, these negatively charged flakes react with various electrophiles (including water) producing functionalized flakes with modified properties [96,99]. Unless negatively charged, graphene is only stable in aprotic solvents under inert conditions and will react otherwise with any electrophile [96,99], while negatively charged nanosheets of TMDs can be stably dispersed in water without reacting with the solvent [85]. However, antibonding d-orbitals of the transition metals are filled leading to flakes with different electronic properties such as transition from semiconducting to metallic in the case of group VI TMDs [85]. Electrochemical intercalation and subsequent exfoliation has recently demonstrated almost defect-free, predominantly monolayer graphene production [100] and it is expected that a similar product quality can be realized in the case of other layered crystals after careful process optimization. Moreover, ion exchange reactions as well as intercalation of organic molecules can result in high quality nanosheets of layered double hydroxides [84] or MXenes [101], respectively. However, these approaches are limited to few layered crystals. In the case of graphene, the intercalation of graphite via acidic chemical reaction produces the widely studied graphene oxide (GO) [99,102,6,103]. GO originates from the oxygenation of graphite to form graphite oxide, which can then be exfoliated by mild agitation to yield stable suspended layers of GO in polar solvents such as water and alcohols [99,102,6,103]. Despite the prevalence of monolayer GO flakes of lateral sizes in the range of 50–100 μm, the GO flakes differ from pristine graphene, bearing a population of functional groups that disrupt the sp^2 structure of graphite [104]. GO treated by chemical or thermal reduction yields reduced graphene oxide (RGO) [99,102,6,103]. However, RGO remains intrinsically defective and never retrieves the pristine graphene properties [104], with different application areas from the ones of graphene and will not be covered by this chapter.

Compared to intercalation, a less chemically aggressive and simpler method for producing 2D crystals in liquids is liquid phase exfoliation (LPE). In this method, the inter-flake energy is overcome by the input of microfluidic, shear or ultrasonic energy in the presence of a stabilizing liquid [40,49,88,29]. The resultant flakes are generally defect-free and free from functionalisation [40,39,49,88,29]. This highly scalable technique can be applicable to a wide range of layered materials and is ideal for fabricating inks [88,89,41,105], pastes [90], composites [36,106,107,87], and coatings [40] for integration, for example, into printed devices [88,89,41].

In this section we discuss the recent advances and remaining challenges in 2D flakes production and dispersion by LPE with an emphasis on recent progress to give a comprehensive, rather than exhaustive, overview of the field. For additional information, the reader is referred to a number of recent review articles [108,80,109,110]. In general, flakes in the resultant dispersions are highly polydisperse (i.e. presence of sheets with various thicknesses and lateral sizes). However, in particular for electronic applications, flakes with consistent properties, hence uniform size and thickness [111,112] distribution are required. Therefore, it will be important to devise strategies to sort 2D flakes according to length and thickness as also summarized. In general, LPE can be considered as a three-step process as discusses in the subsections below: (i) exfoliation of the layered crystals, which provides the energy to overcome the inter-layer attraction forces, (ii) stabilization of the exfoliated flakes in liquid, which ensures uniform distribution of 2D flakes within the dispersion and (iii) the size selection.

2.2.1 Exfoliation of layered crystals

The exfoliation has first been achieved by ultrasonication of bulk layered crystals in appropriate media [108,80,109,110], resulting in 2D flake dispersions with concentrations in the g/L range [113,114]. However, this process is hard to scale up [39], and the ultrasonic intensity decreases rapidly both axially and radially from the probe, strongly restricting the volumes that can be processed [114]. Over the past few years both ball milling [115–117], shear exfoliation [39,118] and very recently microfluidization [40] have been identified as suitable candidates to replace ultrasonication as scalable layered materials exfoliation process.

Ultrasonication: Ref. [119] reported partial exfoliation of graphite by sonication already in 2005, while in 2008 Ref. [49] achieved single layer graphene exfoliation. Exfoliation by ultrasonication is largely induced by cavitation (i.e. the formation, growth, and collapse of bubbles or voids in liquids due to pressure fluctuations) [120]. As a result, the tensile and shear stress generated by collapsing cavitation bubbles acts on the layered material leading to both layer separation and flake fragmentation [121]. Ultrasonic energy can be generated by either sonic baths [49,29,88] or ultrasonic tips [26,112]. In the first case, the ultrasonic intensities acting on the sample are lower than nominally expected and non-uniformly distributed through the tank, resulting in a poor reproducibility of the process [114]. In the second case, high-power sonic probes generate intense ultrasounds directly underneath the probe's tip, therefore the exfoliation will strongly depend not only on ultrasonic power, amplitude, and frequency, but on the sonic probe and vessel shape. Both techniques suffer from poor reproducibility and results in significant fragmentation of the starting material [122], which might affect the scale-up of the exfoliation to industrially relevant quantities. Nonetheless, either ultrasonication techniques are still the most frequently used to produce LPE nanomaterials and mono- and few-layer flakes on the labscale [109,110].

Dispersions of single layer graphene (SLG) flakes can be produced at concentrations $c \sim 0.01$ g/L [49] with a yield by weight $Y_W \sim 1\%$ [49]. Where, Y_W is defined as the ratio between the weight of dispersed material and that of the starting graphite flakes [28]. Dispersions of few layer graphene (FLG) (<4 nm) can be achieved with $c \sim 0.1$ g/L [88] in N-Methyl-2-pyrrolidone (NMP) and $c \sim 0.2$ g/L in water [123]. The low $Y_W \sim 1$–2% [123,88] for FLG in bath sonication is due to the fact that a significant amount of graphite remains un-exfoliated as the ultrasonic intensity (i.e. the energy transmitted per unit time and unit area W/cm^2 [114]) is not uniformly applied in the bath [114,124] and depends on the design and location of the ultrasonic transducers [124]. In tip sonication, the ultrasound intensity decays exponentially with distance from the tip [125], and is dissipated at distances as low as ~1 cm [125]. Therefore, only a small volume near the tip is processed. Refs. [126,90] reported ~2 nm thick flakes with lateral size ~50–70 × 50–70 nm^2 and $c \sim 0.2$ g/L with $Y_W = 1\%$ by tip sonication.

Other layered crystals can also be exfoliated in this way [127,128]. While dispersed nanomaterial concentration is often considered a FOM, a comprehensive study of the ultrasonication processing parameters (such as time, amplitude, power, frequency, vessel shape, etc.) that have an impact on the exfoliation process is still missing. Ref. [129] proposed a model to describe the

fragmentation process of layered materials during ultrasonication [129]. While LPE has been shown to generally result in defect-free flakes, a number of groups have recently demonstrated basal-plane defect formation during cavitation upon longer ultrasonication times [130]. This clearly stresses the importance of further work on the exfoliation mechanism by ultrasonication.

Ball milling: The ball milling technique has been applied to graphite to yield liquid-exfoliated mono- and few-layer graphene [116]. Given the scalability of the process, ball milling is used industrially to grind materials. The exfoliation of layered materials is both driven by shear and compressive forces (from collisions) requiring a careful optimisation to minimize fragmentation of the exfoliated sheets. Compared to ultrasonication, exfoliation by ball milling is a rather young technique that will require further optimization of process parameters such as delamination tool, media size, and stirrer rotation. Two type of mills can be used to achieve exfoliation: stirred media mills and planetary ball mills [121,115,116,131,132]. Several reports have shown mono and few-layer graphene exfoliation [121,115,116,131,132]. In the case of planetary ball mills, longer process times at slower rotations are essential to avoid noticeable fragmentation and introduction of defects onto the exfoliated graphene flakes [115]. Stirred media mills for the production of graphene dispersions in solvent [133] and surfactant media has recently been reported, where process parameters have revealed a strong dependance on viscoelastic propertied of the solvent [134].

On the other side, very little research has been conducted on layered crystals beyond graphene with this technique to date. Ref. [117] used a combination of planetary ball milling and ultrasonication to exfoliate h-BN and molybdenum disulfide (MoS_2) [117]. While ball milling in stirred media mills has been shown to exfoliate TMDs without using additional production techniques [135]. However, further studies will be required to demonstrate the broader applicability of this technique.

Shear exfoliation: Shear exfoliation based on rotor/stator [39,118] or rotating blade mixers [136] has proven a scalable production technique to exfoliate layered crystals. The fluid dynamics during the process is intended to be shear dominated with fragmentation limited to milling by the rotor. Shear exfoliation is currently used in industry and, although limited by the volume of the container, could be a promising production technique for LPE nanosheets in large quantities. Beyond graphene, a number of layered crystals [39,136,121] such as BN [39], TMDs [39] or black phosphorous (BP) [137] have been processed by shear exfoliation. The first reports focused on using rotor/stator mixers [39,136,118], although it was shown [39] that exfoliation can occur even in laminar flow, as long as $\dot{\gamma} > 10^4\ s^{-1}$ act on the layered crystals. For few layer graphene (FLG, <4 nm), the dispersed concentration and production rate was characterized as function of process parameters such as initial graphite concentration, rotor speed, rotor diameter, and liquid volume [39]. Similarly to ultrasonication, a problem associated with rotor/stator mixers is that the exfoliation events are localized in the vicinity of the rotor/stator [39]. On the other side, exfoliation using rotating blade mixers generates turbulent shear throughout the tank and has been shown to increase production rates [118]. However Ref. [39] used a rotor-stator mixer to exfoliate graphite, reaching $C < 0.1$ g/L of FLGs with $Y_W < 2 \times 10^{-3}$% [39]. The low Y_W is because in mixers, high shear rate, $\dot{\gamma} \sim 2 \times 10^4 \times 10^5\ s^{-1}$ (i.e. the velocity gradient in a flowing material) is localized in the rotor stator gap [39,138], and can drop by a factor 100 outside it [139].

Microfluidization: Microfluidization is a homogenization method that applies high pressure (up to 207 MPa) [140] to a fluid forcing it to pass through a microchannel (diameter, $d < 100\ \mu m$), as shown in Fig. 4. The key advantage over ultrasonication and shear-mixing is that the high shear rate ($\dot{\gamma} > 10^{-6}\ s^{-1}$) [40] is applied to the whole fluid volume, and not just locally. Moreover microfluidization can be designed in a cyclic process flow, making the process highly scalable [40].

Turbulent mixing is characterized by a near dissipation-less cascade of energy [141], i.e. the energy is transferred from large random, three-dimensional eddy type motions to smaller ones. This takes place from the inertial subrange (IS) of turbulence where inertial stresses dominate over viscous stresses, down to the Kolmogorov length [142], i.e. the length-scale above which the system is in the inertial subrange of turbulence, and below which it is in the viscous subrange (VS), where turbulence energy is dissipated by heat [141]. During microfuidization of graphite flakes, for example, exfoliation occurs in the IS of turbulence rather than VS, where energy is dissipated through viscous losses. The main stress contributing to exfoliation is due to pressure fluctuations, i.e. the graphite is bombarded with turbulent eddies. In comparison, in a kitchen blender exfoliation occurs in the VS, where the energy is dissipated through viscous losses, rather than through particle disruption. This makes microfluidisation highly efficient in the exfoliation of graphite [40] and a very promising technique for the exfoliation of other layered materials.

Microfluidization was used for the production of polymer nanosuspensions [140], in pharmaceutical applications to produce liposome nanoparticles with $d < 80$ nm [143], or nanoemulsions [144]. Microfluidization was also used for the de-agglomeration and dispersion of carbon nanotubes [140] and more recently for the production of graphene nanoplatelet inks and screen printing pastes [40]. A similar technique known as High Pressure Homogenization (HPH) (a technique which pushes a suspension through a narrow gap at 1500 bar) has been used to help redisperse functionalised thermally reduced graphene oxide in water, acetone and isopropanol however it was not used to exfoliate material [145].

2.2.2 Stabilisation of exfoliated flakes

The presence of a stabilizer is required in LPE. Stabilizers play a dual role: preventing aggregation of the exfoliated flakes and reducing the net energy cost of exfoliation via the stabilizer flake binding. There are three main classes of stabilizers which can achieve this target: solvents, surfactants, and polymers as outlined below. Solvents ideal to stabilise graphene are those that maximize the area of solid/liquid surface in contact, thus minimizing the interfacial tension [mN/m] between the liquid and graphene flakes [63,146]. In general, interfacial tension plays a key role when a solid surface is immersed in a liquid medium [63,146]. If the interfacial tension between solid and liquid is high there is poor dispersibility of the solid in the liquid [63]. In the case of graphitic flakes in solution, if the interfacial tension is high, the flakes tend to adhere to each other and the work of cohesion between them is high (i.e. the energy per unit area required to separate two flat surfaces from contact [63]), hindering their dispersion in liquid. Liquids with surface tension (i.e., the property of the surface of a liquid that allows it to resist an external force, due to the cohesive nature of its molecules [63]) $\gamma \sim 40$ mN/m [49], are the most suitable solvents for the dispersion of graphene and graphitic flakes, since they minimize the interfacial tension between solvent and graphene.

Layered crystals beyond graphene such as h-BN [147], and TMDs [29] can also be exfoliated and stabilized in suitable solvents free from additional additives [29]. A number of solubility parameters such as solvent surface tension (γ), Hildebrandt or Hansen parameters describe stabilization of few layer flakes very well [49,123], as experimentally shown by analyzing the dispersed nanomaterial concentration as function of solubility parameters. Solvent degradation, especially during ultrasonication-based exfoliation will play an effect in the flakes stabilization. For example, it was recently shown that the controlled addition of water and subsequent ultrasonication in a widely used solvents such as NMP and dimethylformamide (DMF) can further increase the dis-

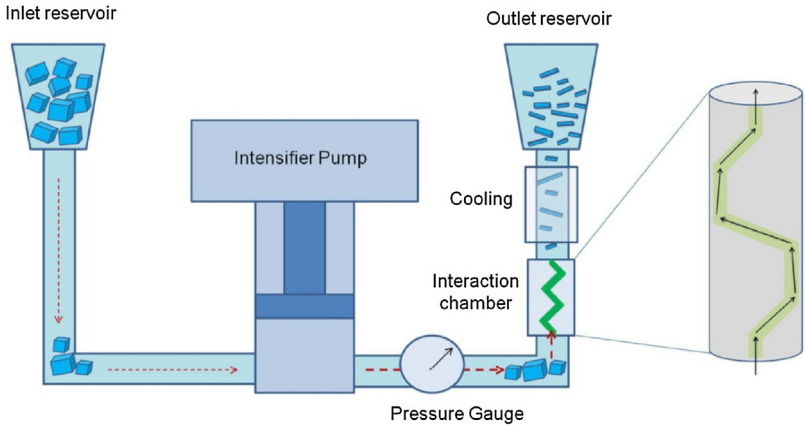

Fig. 4. Schematic of the microfluidization process. Adapted from [40].

persed nanomaterial concentration in the case of MoS_2 [148]. More recently, a wide example of this approach has been demonstrated with the exfoliation and stabilisation of MoO_3 [128], GaS [149] and BP [127,128] confirming the wide applicability of the solvent stabilisation and, like in the case of BP, when unstable layered crystals are exfoliated in liquid, suitable solvents can protect the flake surface significantly slowing down the reaction rates [127].

However, the majority of solvents with $\gamma \sim 40$ mN/m (i.e., NMP, DMF, Benzyl benzoate, gamma-Butyrolactone, GBL) have some disadvantages. E.g., NMP may be toxic for the reproductive organs [150], while DMF may have toxic effects on multiple organs [151]. Moreover, all have high (>450 K) boiling points, making it difficult to remove the solvent after exfoliation. As an alternative, low boiling point solvents [152], such as acetone, chloroform, isopropanol, etc. can be used, however the final stable concentration of solute is orders of magnitude lower than suitable high boiling point solvents. The use of aromatic perylene diimide surfactants [153] have been used with low boiling point solvents such as tetrahydrofuran and chloroform to increase the final stable graphene ink concentration to 0.03 mg/ml however the residual stabilisation agent will remain once deposited which could decrease the performance of the material when used in a final device. More recently Ref. [154] used Poly(3,4-ethylenedioxythiophene)-poly(styrenesulfonate)(PDOT:PSS) as a conductive stabilisation agent to improve the concentration (~0.1 mg/ml) of graphene in a low boiling point solvent (e.g. ethanol) while also improving the performance of the graphene ink in the final application as a TCF for a capacitive touch device [154].

In the quest for the search of alternative safe and sustainable solvents for the LPE process of 2D crystals, a promising approach involves the use of co-solvents to increase the affinity between liquid environment and 2D crystals [155–157]. First experimental attempts by using a mixture of solvents [155], e.g., water/ethanol [155,156], water/IPA [156], etc. have been carried out recently. The rheological properties such as γ, viscosity (η mPa s) and density (ρ; g cm^{-3}) [158] of the mixture can be controlled by adjusting the relative concentration of the co-solvents. However, yield of single layers and the concentration of the exfoliated and stabilised flakes has been reported to be lower with respect to the ones achieved with NMP and diclorobenzene [157]. Another critical point is the stability of the water and alcohols mixtures [159,155,156]. In fact, γ changes non-linearly after the addition of alcohols (e.g. ethanol) to water [158] being also sensitive to solvent evaporation [156]. Moreover, the rheological properties of alcohol-based co-solvents are very sensitive to temperature variation [158], making this a serious problem both during the exfoliation process as well as for the stability of the dispersions or time.

Surfactants: Water has $\gamma \sim 72$ mN/m [63], too high (30 mN/m higher than NMP) for the dispersion of graphene [42] and graphite [42]. In this case, the exfoliated flakes can be stabilized against re-aggregation by Coulomb repulsion using linear chain surfactants, e.g. Sodium dodecylbenzene sulphonate (SDBS) [50], or bile salts, e.g. sodium cholate (SC) [112] and sodium deoxycholate (SDC) [123,160] or polymers, such as pluronic [161]. Linear chain surfactants can stabilize the flakes by noncovalent interaction between the plane of the graphene flake and the surfactant tail group [162]. The polar head group then interacts with the liquid and is responsible for the stabilization of the flakes in dispersion [162], while the electrostatic and steric repulsion prevents flakes reaggregation [112,50,123]. In the case of ionic surfactants [163], i.e., anionic, cationic, zwitterionic, the repulsion is due to the interaction between the charge distributions of surfactant coatings adjacent flakes. Alternatively, layered crystals can be exfoliated in non-ionic surfactants or polymers where stabilization is mainly due to steric repulsion [50]. Graphene and other 2D crystals result stable in either organic or aqueous media, through non-ionic surfactants [164]. In this case the polymer adsorbs on the surface of the flake at a number of sites with many loops and tails protruding into the solvent [164,161]. When two flakes approach each other, the polymer chains begin to occupy the same space, the number of chain confirmations falls, resulting in an increase in the free energy of the system [165] and this generates a stabilizing repulsive force [165]. An added value of using polymers is that η can potentially be tuned by the polymer concentration (e.g. in microfluidization) and that composites can easily be formed [36,106,40]. However, depending on the final application, the presence of surfactants/polymers may be an issue, e.g. compromising, decreasing, the inter-flake conductivity [152].

After the exfoliation step, the as-produced dispersions have an heterogeneous composition of exfoliated sheets both in lateral size and thickness. However, this is not the ideal condition to fully exploit the properties of the exfoliated 2D crystals, in view of any application ranging from mechanical to electronic and electrochemical. Thus, the full control of the morphological properties is a fundamental goal to be achieved in the short term. Thick flakes can be removed by different strategies based on ultracentrifugation in a uniform medium [166], or in a density gradient medium (DGM) [167]. The first is called differential ultracentrifugation (sedimentation based-separation, SBS) [166], while the second is called density gradient ultracentrifugation (DGU) [167]. While the SBS process separates various particles on the basis of their sedimentation rate [166] (in response to centrifugal force acting on them), during DGU the flakes are ultracentrifuged in a preformed DGM [167,168] where they move along the cuvette until they reach the

corresponding isopycnic point, i.e., the point where their buoyant density (i.e. the density, ρ, of the medium at the corresponding isopycnic point) equals that of the surrounding DGM [167].

SBS is a highly common separation strategy for graphene [169] and other 2D crystals, to date [109,170]. Flakes ranging from few nanometers to a few microns have been produced, with concentrations up to a few mg/ml [169]. However, enrichment of thin and single layer flakes may be challenging, unless they are very small in lateral dimensions hence with a low sedimentation coefficient values. On the other hand, control on the number of layers can be achieved via DGU, where a uniform and well controlled surfactant/polymer coverage of the flake is required [112] as the stabilization layer also contributes to the buoyant density. This will result in slight variations of the buoyant densities of SL and few-layer nanosheets which can lead to spatial separation in a centrifuge cell if the density gradient is well matched to these subtle differences [112]. However in the case of 2D crystal separation, monolayers flakes and bulk layered crystals have the same ρ, second, the large majority of 2D crystals have higher density (e.g., MoS_2, $\rho = 5.06\,g\,cm^{-3}$, WS_2, $\rho = 7.5\,g\,cm^{-3}$, WSe_2, $\rho = 9.32\,g\,cm^{-3}$), than the common DGM (e.g., Iodixanol $\rho = 1.32\,g\,cm^{-3}$) [28] making the process highly challenging and affecting the reproducibility of the results.

2.3 Formulation: from dispersion to ink

The dispersions of single and multi-layer 2D crystals produced by LPE have a great potential to be employed in numerous coating and printing methods. In many cases, the dispersion differs from a printable ink and the composition of functional inks strongly depends on the type of deposition/printing process. This requires an accurate and tailored step of ink formulation. In this section we will review the formulation of inks made with 2D crystals for their application in printed and flexible electronics, which is a rapidly emerging platform in the electronics industry [171]. We will present the development process and the key parameters enabling the full exploitation of 2D crystal-based inks for, drop [172], spin [94] and spray [95] coating, inkjet [88,41,89], gravure [173], screen [90,91,40] and flexographic printing [174]. Furthermore we will discuss the production of printed hybrid heterostructures of different 2D crystals films one on top of another one [32,175,176]. This approach could pave the way to an all printed 2D crystals based electronics enabling a variety of new opto-electronic devices, with the added value of reduced cost. We will also briefly summarize the role of printing technologies for the realization of novel 2D crystal based devices having lightweight, foldable, and flexible designs and superior electrical, optical and mechanical properties with respect to the state-of-the-art.

3 Printing and coating of 2D crystal-based inks

Material films can be deposited using many techniques summarized in Table 1 although some of these techniques have clear advantages as they allow for precise patterning. Furthermore some of the deposition techniques are extremely suitable for scale up due to their applicability in roll to roll processing such as flexo, gravure and spray coating. Other techniques also have their merits, inkjet printing for example has a high resolution (~50 μm) which is difficult to reach by other scalable solution processing techniques. For all of these techniques the ink properties, in particular the viscosity needs to be tuned to fit the printing process that will be used. For example screen printing requires a viscosity >1000 mPa s typically only achieved with the addition of a rheology modifier. If the electrical properties of the ink are significantly important for the final application, techniques such as inkjet or spray coating can be used which do not necessarily require additional modifiers to adjust the ink properties (i.e. viscosity or surface tension). In the next section we will focus on the most commonly used deposition techniques for simplicity.

3.1 Spin coating

Spin coating has proven to be an effective direct deposition tool of novel nanomaterial-based inks such as, quantum dots [177,178], metal nanoparticles [179,180], CNTs [181,182], as well as 2D crystals such as RGO [94,43], TMDs [183,135] onto rigid or flexible substrates. Spin coating of 2D crystal-based dispersions [94,43,183,135] has been developed for the realization of electrodes for photovoltaic [94,43,183,135], micro-supercapacitors [184], or field emitters [94], where the thickness and homogeneity control of the electrode itself play a crucial role. For example, Ref. [43] demonstrated the preparation of RGO films by spin coating with a thickness of 20 nM having a R_s of 2 kΩ/□ and a transparency higher than 70%. The as produced film was then used as TC electrode in organic solar cells (OSCs) [43]. MoS_2 sheet-based films prepared by spin coating were instead used as hole transport layers in OSCs [183]. Micropatterned spin-coated RGO films, having a thickness in the 6–100 nm range have enabled in-plane interdigital micro-supercapacitors on both rigid and flexible substrates [184]. Due to the high electrical conductivity (i.e. $\sigma = 345\,S\,cm^{-1}$), of the fabricated RGO films and the in-plane geometry of the microdevices, the as-prepared micro-supercapacitors deliver a remarkable power density of $495\,W\,cm^{-3}$ and an energy density of $2.5\,mW\,h\,cm^{-3}$, which is comparable to that of lithium thin-film batteries [184].

3.2 Blade and rod coating

Blade-coating has proven useful to deposit about 10 μm films of graphene and reduced graphene oxide inks to make electrodes for graphene-based supercapacitors, with the primary goal of developing a one-step manufacturing technique for graphene supercapacitors on an industrial scale. Both with gelled electrolyte and liquid electrolyte supercapacitor reaching a maximum capacitance of $33\,mF\,cm^{-2}$ and $52\,mF\,cm^{-2}$ respectively [185].

Graphene/epoxy paste deposited by doctor-blade coating have been used in a flexible piezo-resistive sensor reporting a gauge factor of ~13 and a stability of up to 1000 cycles [186]. More recently blade coating has been used to coat graphene-based solar cells onto polyester fabrics generating solar energy harvesting textiles with power conversion efficiency of up to 2.27%. Rod coating is one of the most practical techniques for graphene and 2-d material inks deposition. Transparent conducting electrodes prepared by rod-coating hybrid graphene and doped-SWNT inks on PET have shown a sheet resistance $R_s \sim 1000\,\Omega/\square$ and optical transmittance T, of above 90% [34]. Also GO prepared by Hummers method had been coated onto PET by Meyer rod followed by subsequent reduction in HCl/H_2 [187]. The flexible transparent conducting RGO film showed $R_s \sim 1800\,\Omega/\square$ and optical transmittance, T of above 81%. Similarly rod-coated RGO films on glass have been demonstrated as de-icing layer with a $R_s \sim 5600\,\Omega/\square$.

3.3 Spray coating

Spray coating (shown in Fig. 5) is a versatile technique for large area deposition of highly uniform films of graphene and 2D-materials. Spray coating of GO inks on Si/SiO_2 [188] and quartz [189] has been used to demonstrate field effect response with a mobility of $\sim 1\,cm^2\,V^{-1}\,s^{-1}$, and transparent conducting films with $R_s \sim 2.2\,k\Omega/\square$ and $T \sim 84\%$, respectively. A colloidal mixing of MnO_2-RGO and carbon fibre paper has been shown to produce high-performance supercapacitors with a specific capacitance of

Table 1
Summary of film forming methods compared in terms of the ink viscosity required, speed of the printing process, possibility of patterning the deposited film, typical thickness of deposited film and the area of deposition.

Technique	Ink viscosity	Speed	Film thickness	Area of deposition	Pattern
Drop casting	1–1000 mPa s	Low (cm^2/h)	<100 nM	<1 m^2	Possible
Spin coating	<10 mPa s	Low (cm^2/h)	<100 nM	~ 0.04 m^2	No
Bar coating	1–1000 mPa s	Low (cm^2/h)	<100 nM	<1 m^2	Possible with mask
Doctor blade	1–1000 mPa s	Low (cm^2/h)	>100 nM	<1 m^2	Possible with mask
Vacuum filtration	<10 mPa s	Low (cm^2/h)	>100 nM	~0.01 m^2	Possible with mask
Screen printing	>1000 mPa s	High (m^2/h)	>1000 nM	>1 m^2	Yes
Inkjet printing	1–10 mPa s	High (m^2/h)	<100 nM	>2000 μm^2 - >1 m^2	Yes
Spray coating	1–100 mPa s	High (m^2/h)	<100 nM	>1 m^2	Possible with mask
Flexographic printing	>200 mPa s	High (m^2/h)	>100 nM	>1 m^2	Yes
Gravure printing	>200 mPa s	High (m^2/h)	>100 nM	>1 m^2	Yes

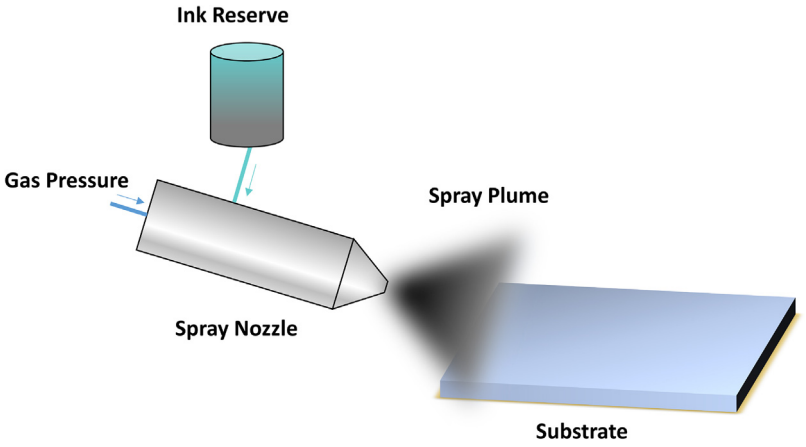

Fig. 5. Schematic of the spray-coating process which can be used to deposit 2D crystal-based inks onto a substrate using a spray gun. Adapted from [194].

393 F g^{-1} and a capacity retention of over 98.5% [190]. Dye sensitized solar cells using spray coated hybrid GO-Pt as counter electrode [191] have achieved a power conversion efficiency of 6.77% on quartz and 4.05% on flexible plastic substrate. Also, PDOT:PSS has been used in combination with graphene to create hybrid graphene-PDOT:PSS inks subsequently used as bottom electrodes in organic photodetectors achieving a detectivity (D) of 1.33×10^{12} Jones which is of the same magnitude as that of reported state-of-the-art solid state inorganic photodetectors [192]. Spray coated MoS_2 layers have been mostly used as super-hydrophobic coatings [193] in a blend with polyurethane or anti-flame retardant. More recently hybrid PDOT:PSS/graphene inks have been spray coated on three-dimensional objects such as a poly(methyl methacrylate) sphere to create an TCF electrode 10^4 S/m) which could be used in a semi-transparent (65%) capacitive touch device [154]. It was also found in this work that the spray coating uniformity could be improved by minimising the ink surface tension (~30 mN/m) and boiling point (~79 °C), while the optimum spraying temperature was at room conditions (20 °C) [154]. Thin film uniformity is essential in spray coating to build devices such as solar cells, OLEDs, field-effect transistors, saturable absorbers and TCFs to reduce defects, improve field-effect mobility or device efficiency or even just to achieve a simple percolating film [154].

3.4 Screen printing

Screen printing is a highly common technique for the deposition of thick layers (~25 μm) through a pre-patterned mask. Printed supercapacitors with specific capacitance of 269 F g^{-1}, power density of 454 kW kg^{-1} and energy density of 9.3 Wh kg^{-1} have been printed using graphene nanoplatelets/polyaniline electrodes blend [79]. Electric field emitters from RGO electrodes from a blend of GO, ethylcellulose and terpineol have been screen printed on glass. The presence of graphene flakes protruding out of the film enabled a field enhancement factor of ~4500 and a threshold field of ~1.5 V μm^{-1} [195]. Graphene-based screen printed electrodes can be deposited with a resolution of ~5 μm and a conductivity $\sigma \sim 1.8 \times 10^4$ S/m and used as source drain contact in a fully printed and flexible TFT [90]. In 2014 screen printed GO ink reduced after deposition on fluorine-doped glass substrate has been demonstrated as counter electrode in dye sensitized solar cells achieving a total power conversion efficiency of 5.19% and estimated energy consumption per unit area of 1.1 kJ cm^{-2} [118]. Recently mass produced inks of graphene nano platelets prepared by microfluidic exfoliation in water-based solution have been screen printed on paper (Fig. 6 a), achieving $\sigma \sim 2 \times 10^4$ in a touch-pad array configuration (Fig. 6b and c) [40].

3.5 Ink-jet printing

Inkjet printable conductive inks based on nanomaterials have been formulated, ranging from metal nanoparticles [196] to organic semiconductors [197] and CNTs. However, silver and copper nanoparticles for example [18], exploited for the formulation of conductive inks, are expensive and not stable in most common solvents (e.g., water, acetone, IPA, ethanol), thus requiring stabilizers for their dispersion in such solvents which severely affect their implementation [198,67]. Furthermore, metal-nanoparticle based inks show a tendency toward oxidation [198,67], and high temperature sintering post-processing is often required [199]. Organic semiconductor inks [138], used mainly for the realization of organic TFTs, have low charge carrier mobilities ($\mu \sim 1$ cm^2 V^{-1} s^{-1}) [200], while CNTs suffer electrical heterogeneity (being a combination of metallic and semiconducting) [201], and high contact resistance between the individual CNTs.

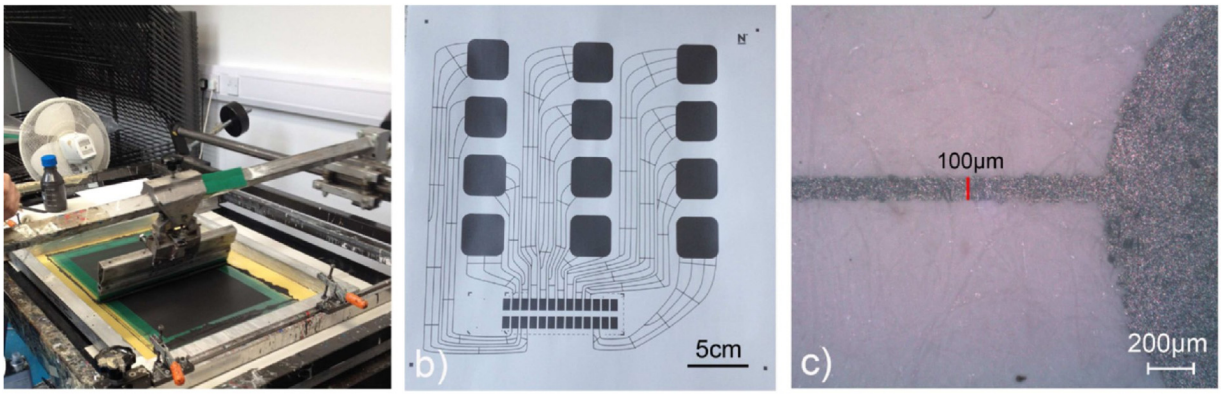

Fig. 6. (a) Demonstration of screen printing of the graphene ink, (b) capacitive touch-pad design printed on paper, (c) with a line resolution of 100 μm. Adapted from Ref. [40].

Several groups reported GO-based inks [202,42,198]. Ref. [202] ink-jet printed RGO films for sensors applications, while Ref. [198] produced RGO-stabilized Cu nanoparticles as low temperature metal colloids, to replace standard metal nanoparticle inks, that require high temperature sintering postprocessing [199]. Torrisi and coworkers [88] reported the first ink-jet printed graphene transparent conducting films and TFT using LPE graphene ink in NMP and NMP/Ethylene Glycole, achieving a field effect mobility of up to 95 $cm^2 V^{-1} s^{-1}$ and ON/OFF ratio of up to 10. Similar mobilities (~90 $cm^2 V^{-1} s^{-1}$) have been achieved for highly reduced GO films by ink-jet printing [42], with an ON/OFF ratio up to 10 [42].

The formulation of functional inks based on pristine LPE graphene sheets is mostly driven by the requirements set by the choice of solvents able to disperse the sheets in addition to the aforementioned constraints related to the ink printability [203–205,67], thus limiting the selection/choice of suitable solvents, as discussed in Section 2. The initial attempts [88,89] exploited graphene inks prepared in NMP [88] and DMF and subsequent solvent exchange with terpineol [89], respectively, to print conductive stripes reaching $R_s \sim 30\,k\Omega/\square$ on glass substrates. In Refs. [88,206,126] the authors printed graphene ink on rigid substrates (glass [206] and SiO_2 [88,126]) previously treated with hexamethyldisilazane (HDMS), to prevent undesired coffee-ring effects of the printed features. Refs. [206,126] thermally annealed the as-printed graphene stripes at temperatures higher than 250 °C, achieving $R_s \sim 1.3\,k\Omega/\square$. Fig. 7a–c shows some examples of inkjet printed drops of graphene ink on Si/SiO_2 and HMDS modified Si/SiO_2, and time evolution of drop-jetting (Fig. 7d).

Co-solvent mixtures have also been proposed as an alternative solution to minimize the coffee-ring effect [159]. In this case the LPE graphene ink is designed in a solution of two miscible solvents, causing a higher enthalpy of vaporization (ΔH_{vap} [kJ mol^{-1}]) than water, resulting in less coalescence [156,158]. Conductive stripes with $R_s \sim 13\,k\Omega/\square$ have been achieved ink-jet printing a graphene ink in water/ethanol mixtures on PET [159]. Recently, $R_s \sim 1$–$2\,k\Omega/\square$ was reported for graphene films ink-jet printed by graphene ink in ethylene glycol mixed with a copolymer of NMP and vinyl-acetate on polymer-coated paper [105]. Ref. [41] used a graphene ink in NMP to print conductive stripes on PET foils coated with aluminum oxide and poly(vinyl alcohol) to reduce substrate-related drying problems.

Recently, Ref. [207] proposed a general route to efficiently integrate graphene inks as well as other 2D crystals (e.g., MoS_2, WS_2) with the ink-jet printing technology, overcoming several still existing drawbacks for a reliable mass production of high-quality 2D crystal-based films/patterns as described below. The process relies on a distillation-assisted solvent exchange in combination with polymer stabilization (ethyl-cellulose (EC), $\eta = 4$ and 22 mPa s) [207]. This enabled them to formulate an environmentally friendly and printable MoS_2 ink consisting of MoS_2 few-layers (>6 layer by Raman investigation, 5.7 nm thick by cross-sectional profile analysis) in terpineol [207]. The MoS_2/terpineol ink rheology was tuned with ethanol (EtOH) ($\eta_{EtOH} \sim 1$ mPa s, MoS_2 concentration ~1 mg mL^{-1}) and stabilized with EC polymer to allow for optimal jetting and printing resolution (droplet diameter or line width) of ~80 μm on Si/SiO_2 substrate [207]. MoS_2 and graphene inkjet printed photodetectors have been demonstrated in a planar (non-heterostructure) configuration in 2014 [41], achieving a photoresponsivity of few μA W^{-1}. Graphene, WS_2, MoS_2, and BN inks deposited via drop-casting, inkjet printing, and vacuum filtration have been combined with graphene grown by chemical vapour deposition (CVD) [46] for the realization of heterostructures.

However, both the deposition methods used and the rheological characterization of the inks was not clear and the concentration of the obtained dispersion appeared to be low compared to average standards in inkjet printing (WS_2 = 0.04 mg mL^{-1}, MoS_2 = 0.05 mg mL^{-1} and BN = 0.1 mg mL^{-1}). More recently, Ref. [176] reported the formulation of biocompatible graphene, WS_2 and MoS_2 water-based inks stabilized by 1-pyrenesulfonic acid sodium salt and propylene glycol. Inkjet printed graphene/WS_2 heterostructures as well as inkjet printed WS_2 combined with CVD-grown graphene have been used as photodetectors on SiO_2 and PET substrates achieving a photoresponsivity higher than 1 mA W^{-1} (however it remains unclear whether which of the two structures reaches such a value and what performance enhancement the WS_2 and MoS_2 provides) and a read only memory (ROM).

Despite this progress, several issues need to be still overcome for the optimization of 2D crystal-based inkjet printing. The main problem is that the common solvents used in LPE (e.g., DMF and NMP) are toxic and have very low η (<2 mPa s), the latter strongly decreasing the jetting performance. A second issue is the deposition of uniform and pinhole-free thin dielectric films for top-gate TFTs, this is currently limiting reproducible all inkjet printed TFTs based on 2D crystal-based inks. In addition, alignment of the nanosheets needs to be improved in order to increase the film uniformity and retain uniform dielectric properties. Another issue to be faced, is the required post-processing annealing for solvent removal [208], which poses severe limitations to the type of substrate to be used for the printing process. Similar issues are also faced in the case of 2D crystal-based inks prepared in aqueous solution, where the surfactants/polymers removal requires thermal and/or chemical treatments [209], which are often not compatible with the substrate.

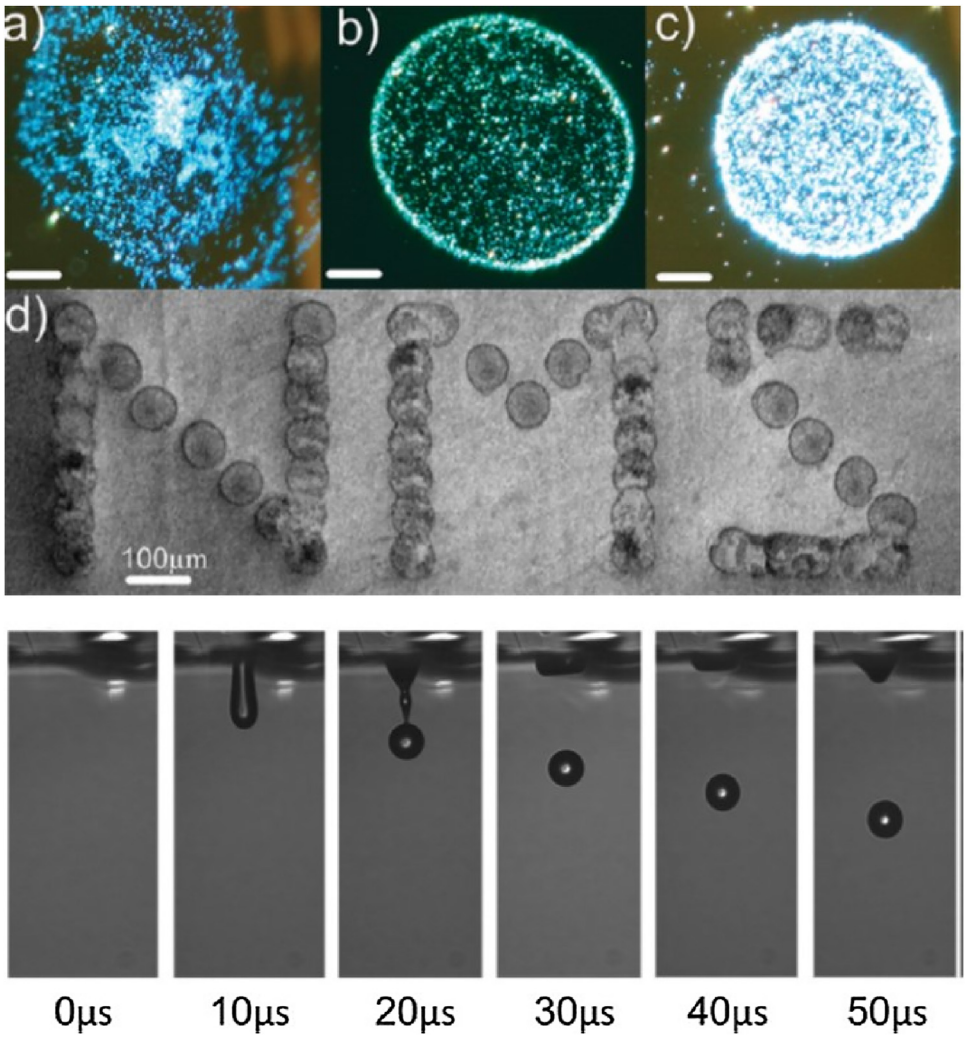

Fig. 7. (a–c) Optical micrograph of graphene inkjet-printed drops on various substrates. Scale is 20 μm. (d) SEM micrograph of graphene ink-jet printed pattern. (d) Photosequence of single drop ejection of graphene ink from an printing nozzle. Adapted from Ref. [88].

Finally most of the 2D crystals inks are formulated in high boiling point solvents (e.g. NMP, DMF, o-DCB) [29]. While this is excellent for dispersing 2D flakes, it results an issue for printed 2D crystal-based heterostructures, as residual solvent (if not evaporated) can result in a re-dispersion and transportation of material on heterostructure interfaces which causes inhomogeneity. Ref. [32] recently proposed a solution to several of these issues by demonstrating ink-jet printed 2D crystal heterostructures using a low boiling point graphene ink in ethanol, formulated by solvent exchange from a graphene solution in NMP and a water-based dielectric h-BN ink, stabilised by Carboxy-methyl cellulose. The heterostructure succesfully operated as an all-printed TFT and integrated circuits with mobility $\mu > 150\,cm^2\,V^{-1}\,s^{-1}$.

3.6 Characterisation techniques

The characterisation techniques used in printed electronics based on 2D crystals can be divided in the ink characterisation and the dry film characterisation on the substrate.

The ink characterisation aims to provide a full understanding of the overall materials content, chemical and physical structure of the flakes, rheology and viscoelastic properties of the formulation. Based on the characterisation techniques for LPE graphene dispersions [49,50], Ref. [88] established a characterisation protocol for graphene inks based on UV-ViS optical absorption spectroscopy (OAS), high-resolution transmission electron microscopy (HRTEM), electron diffraction, and Raman spectroscopy statistics. Atomic force microscopy has also been introduced [100] to characterise graphene and TMDs. Additionally, Ref. [111] introduced photoluminescence excitation spectroscopy as a mean to identify the number of layers in MoS_2 and other TMDs [210] as well as black phosphorous [128]. OAS can be used to estimate the concentration of graphene [49,50,109] via the Beer-Lambert law, according to the relation $A = \alpha c l$, where A is the absorbance, l [m] is the light path length, c [g/L] is the concentration of dispersed graphitic material, and α [$L\,g^{-1}\,m^{-1}$] is the absorption coefficient. The value can be experimentally determined by filtering a known volume of dispersion, e.g. via vacuum filtration, onto a filter of known mass [49,50,109], and measuring the resulting mass using a microbalance.

Thermogravimetric (TGA) analysis is also used to determine the weight percentage of 2D crystals in it, thus enabling the measurement of c [49,50]. However, different values of α have been estimated for graphene [49,50,169,39] and various 2D materials [170,211,212,111] both for aqueous [50,169,111,39] and non-aqueous-based dispersions [170,211,49]. In graphene the optical absorption spectrum is mostly featureless, as expected due to linear dispersion of the Dirac electrons [213,34], the peak in the UV region being a signature of the van Hove singularity in the graphene density of states.

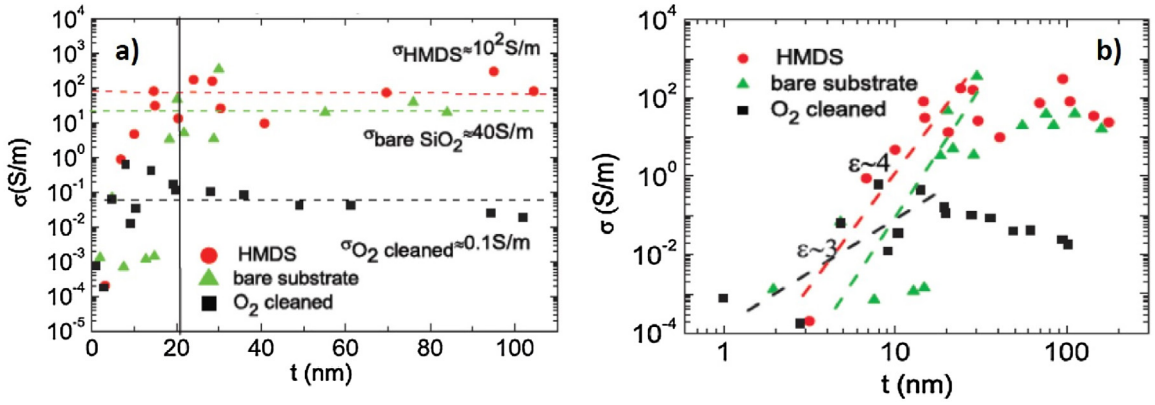

Fig. 8. σ as a function of thickness (t) in (a) linear and (b) logarithmic scale for inkjet printed graphene ink on various substrates (HMDS-coated, O_2 plasma-treated, and pristine Si/SiO_2 substrates. Adapted from Ref. [88].

Ref. [49] derived $\alpha \sim 2460\,mL\,mg^{-1}\,m^{-1}$ for a variety of solvents, i.e. NMP, DMF, GBL, while later Ref. [169] reported $\alpha \sim 3620\,mL\,mg^{-1}\,m^{-1}$ for NMP and Ref. [113] gave $\alpha \sim 1390\,mL\,mg^{-1}\,m^{-1}$ for aqueous dispersions with sodium dodecylbenzene sulfonate (SDBS). This discrepancy has been assigned to the c difference of the two dispersions [113]. However, α cannot be dependent on c. For other 2D crystal dispersions, Ref. [29] reported $\alpha \sim 3400\,mL\,mg^{-1}\,m^{-1}$ for MoS_2, $\alpha \sim 2756\,mL\,mg^{-1}\,m^{-1}$ for WS_2 and $\alpha \sim 2367\,mL\,mg^{-1}\,m^{-1}$ for h-BN. Also Ref. [170] reported $\alpha \sim 1020\,mL\,mg^{-1}\,m^{-1}$ for MoS_2. In order to gain further insights on the actual values of α Ref. [214] derived a relationship between α and the intrinsic 2D crystal absorption obtaining $\alpha \sim 4237$ mL $mg^{-1}m^{-1}$ for graphene, $\alpha \sim 7719\,mL\,mg^{-1}\,m^{-1}$, for MoS_2 $\alpha \sim 3429\,mL\,mg^{-1}\,m^{-1}$ for WS_2 and $\alpha \sim 1161\,mL\,mg^{-1}\,m^{-1}$ for $MoSe_2$. However further investigation is needed to confirm these values experimentally. OAS can also be used to determine the mean length and thickness [nm] of the TMDs such as MoS_2 [111] and WS_2 [210].

A combination of HRTEM and AFM is normally used to determine the yield by SLG percentage Y_M [%] [49,50,88]. In TEM, the number of layers in a flake can be counted both analyzing the edges [49,215] of the flakes and by using electron diffraction patterns [49,216], the latter can easily discriminate between SLGs and BLGs [216], but a more complex analysis is needed for other 2D crystals [29]. AFM enables the estimation of the number of layers by measuring the height of the deposited flakes and dividing by the graphite interlayer distance. However, the estimation of a SLG height via AFM is dependent on the substrate, going from a height of ~1 nm [217] on SiO_2 to ~0.4 nm on mica [218]. Raman spectroscopy is also used for the determination of Y_M and to corroborate the results obtained with TEM and/or AFM. The evolution of the Raman spectrum of graphene and FLG with the number of layers is captured in the changes of the lineshape of the 2D peak and the peak-position changes of the G peak [215,88,219]. PLE can be used in combination with OAS and AFM/TEM statistics to confirm the Y_M and the number of bi- and multi-layer flakes in TMDs, such as MoS_2 [111] and WS_2 [210], as well as in BP [128]. The correlation of the excitonic peaks in TMDs with the number of layers allows confirmation of the various multi-layer fractions. The rheological and visco-elastic characterisation relies on the measurement of the γ, ρ, η, elastic (G') [Pa] and loss (G'') [Pa] modulus. 2.1 Ref. [88] reported surface tension for graphene-NMP ink by the DuNouy–Padday technique [220]. This consists in using a rod of few millimeters in diameter, immersed in the dispersion and then pulled out. The rod is attached to a scale or balance via a thin metal hook that measures the maximum pull force. This is recorded as the probe is first immersed 1 mm into the solution and then slowly withdrawn. The γ of the ink can also be estimated by using the pendent drop method. The shape of the drop suspended from a needle results from the relationship between the surface tension and gravity. The surface tension is then calculated from the shadow image of a pendant drop using drop shape analysis [14]. As discussed in Section 2.3 microbalance [88] or thermogravimetric analysis [40] can be used to determine δ while η, G' and G'' can be determined by rheometers [221] operating with the parallel plate or cup method [221,40,222]. G', represents the elastic behavior of the material and a measure of the energy density stored by the material under a shear process [221], while the loss modulus G", represents the viscous behavior and a measure of the energy density lost during a shear process due to friction and internal motions [221]. The rheological and viscoelastic properties vary largely according to the printing technique as discussed in Section 2.1.

In the dry film characterisation the morphological, electrical, optical and adhesion properties of the printed 2D crystal-based patterns are assessed on the target substrate. The morphology of the printed patterns is assessed via measurement of the film thickness (normally as a function of printing passes in inkjet printing) [88,41,126], the width [173,40] (which in the case of gravure printing depends linearly with the cell size [173]) and the roughness (in terms of R_q or R_a) [88,46]. Optical or stylus profilometry can be used to determine the thickness, width and length of screen, gravure or flexographic printed patterns [40,173]. However, due to limited resolution of profilometer below 1 μm [223], AFM is preferred for determination of the surface roughness of the film [40,88]. AFM can also be used to determine width and length of the patterns [207,41]. The electrical characterisation of the thin films involves the determination of the film R_s and σ performed using a four-point probe system in a Kelvin method [88,40] (four equally-spaced probes in line) [224]. In 2D crystals printed thin films the percolation threshold separates a percolative region denoted by σ scaling as t^{ϵ}, where t is the film thickness and ϵ is the percolation exponent (normally 1–3 for 2D particles) from a region of bulk conductivity where σ is independent of t (Fig. 8a and b) [225,226,88]. The percolation exponent can normally be estimated from a plot of σ vs t as in Fig. 8b [88,225].

The electric field response of the printed graphene thin films is assessed in terms mobility and current on/off ratio from the output and transfer characteristics of printed TFTs [88,227,89]. While TFTs have been demonstrated both in top [227] and bottom-gate [88,89] configurations for graphene printed TFTs, further efforts are required to achieve field effect modulation from 2D crystal printed TFTs. The reported large number of sub-gap trap states in 2D crystal-based thin films from LPE [228] and the variable-range hopping dominated transport might affect the modulation of the charge

carriers concentration in the TFT channel [228]. Finally, the optical absorbance of the printed 2D crystal printed patterns can be measured by OAS operating in transmission [41] or reflectance mode [173]. Ref. [88] proposed a laser-assisted transmittance measurement of graphene printed patterns achieving sub-10 μm resolution.

4 Applications

We present a table listing the key applications of 2D crystal-based inks for the fabrication of printed electronic and optoelectronic devices, sensors, solar cells, batteries and supercapacitors, summarized in Table 2 for pristine graphene devices and Table 3 for the other 2D materials such MoS_2, WS_2 and h-BN.

4.1 Printed electronics

Market forecasts the expansion of large-area printed and flexible electronics reaching more than $70 Bn [229]. The main focus in this arena is on the need for a high mobility (>20 $cm^2 V^{-1} s^{-1}$) and high current on/off ratio (>10^6) at room temperature and ambient atmosphere on flexible substrate, required to drive active matrix display [230]. While in the case of electronic circuits on/off ratios of least >10^3 with mobilities >10 $cm^2 V^{-1} s^{-1}$ will be required to create inverters with signal gains greater than 1. The current state of the art devices have μ ranging from 0.01 to ~1 $cm^2 V^{-1} s^{-1}$, with ON/OFF ratios up to 10^5 [231–233]. Several inkjet printed TFTs using various carbon nanomaterials have been reported. For example, fullerene-based TFTs were discussed in Refs. [234,235], with μ up to 0.01 $cm^2 V^{-1} s^{-1}$ and an ON/OFF ratio <10. TFTs printed from CNT-based inks have been presented by several groups [236,237,17,238,239]. The highest μ reported thus far is ~50 $cm^2 V^{-1} s^{-1}$ combined with an ON/OFF ratio of 10^3, but measured at 10^{-6} Torr [239]. Ink-jet printed TFTs from GO-based inks were discussed in Refs. [202,42], with μ up to ~90 $cm^2 V^{-1} s^{-1}$ for an ON/OFF ratio of 10 (measured at room conditions), after GO reduction. Organic semiconducting inks [231–233] suffer from low μ, limited by variable range hopping of charges between isolated polymer chains [240]. The overall charge conduction in crystalline organic semiconducting thin films is determined by both intra-chain and inter-chain charge transport [241]. The former is much faster than inter-chain hopping [241,240]. Many groups have tried to improve inter-chain hopping [242,243,236,237]. Ref. [242] proposed a chemical modification of the semiconducting organic ink by electron acceptors, while embedding Au nano-particles in the semiconducting organic ink was proposed in Ref. [243]. Embedding CNTs in the semiconducting ink [236,237] allowed to get μ ~ 0.07 $cm^2 V^{-1} s^{-1}$ at room conditions. Despite the relevant improvement of hybrid nanomaterial/polymer composite inks, hybrid structures still lie below the required parameters for active matrix displays.

The on/off ratio in organic polymers is mainly determined by the energy difference between the lowest unoccupied molecular orbital (LUMO) and the highest occupied molecular orbital (HOMO). Moreover the presence of trap states determined by defects in the polymer structure or Peierls instabilities in the polymer 1D structure might affect the reliability of the on/off ratio [244]. Layered and 2D crystals, such as TMDs [245,246], BP [247] as well as other newly reported materials (e.g. Franckeite) [248] are excellent inorganic semiconducting materials, and a large number have shown long term-stability in ambient condition. Single or multilayer MoS_2 TFTs exhibit outstanding performance metrics, including high on/off-current ratio (~10^7), high mobility (~100 $cm^2 V^{-1} s^{-1}$) and low subthreshold swing (~70 mV $decade^{-1}$). These 2D crystals can be formulated into printable inks [88,53,207] making them highly promising for printed electronics and particularly TFTs [53,30]. Inkjet-printed TFTs have been demonstrated with RGO as printable ink [42,202]. Refs. [88,227,126,89] demonstrated graphene inkjet-printed TFTs with μ as high as ~120 $cm^2 V^{-1} s^{-1}$ [227].

However the on/off ratio in graphene printed TFTs is in the 2–10 range [88,53,89]. For this reason, Torrisi et al. [88] also demonstrated the combination graphene/organic polymer Poly[5,5′-bis(3-dodecyl-2-thienyl)-2,2′-bithiophene] (PQT-12), obtaining TFTs with μ ~ 0.1 $cm^2 V^{-1} s^{-1}$ and an on/off ratio ~4×10^5 showing the potentiality of hybrid polymer/2D crystal inks for high-performance printed electronics. In analogy with the TFTs made from single 2D crystal flakes, tremendous efforts are devoted to demonstrate field effect response from 2D crystal based inks. Inkjet printed MoS_2 films onto SiO_2 substrate showed low on/off ratio of ~2, and $\sigma \sim 8.9 \times 10^{-5}$ S/m [207]. However, exciting prospects in this area undoubtedly lie ahead.

4.2 Printed optoelectronics

There are many applications that can exploit the optoelectronic properties of 2D crystal-based inks. For example, in the field of transparent conducting films (TCFs) and electrodes, there are a number of every-day applications, such as smart windows (i.e., electrically switchable optical shutters) [171], electromagnetic shielding [249], electrochromic windows [249], static dissipation [249], defrosting and oven windows [249], that could make use of, for example, graphene-based TFCs. Considering that the majority of these applications do not require very low R_s (~200–400 Ω/□ [250]), LPE graphene could be the right candidate to replace conventional costly and brittle materials such as ITO [249] for many of these applications, due to the ease of fabrication and low cost. However, the key requirements for TCFs in higher-end applications, such as photovoltaic devices or liquid crystal displays are R_s < 10 Ω/□ and T>90% [251]. TCFs produced by inkjet, gravure, and screen printing have not yet demonstrated acceptable values of R_s and T. Thus, future research will be necessary to reveal whether the achievement of such performances will be possible. Importantly, the use of spray and/or rod coating is likely the best strategy for TCFs production [28], not having issues linked to the limited lateral size of the graphene sheets (e.g clogging of the nozzle, size of ink wells in anilox, etc.) affecting the printing process, and to the thickness of the printed feature (>500 nm), typical of gravure and screen printing [11]. Ref. [252] reported a photoresponsivity of ~36 μA W^{-1} from an inkjet printed MoS_2 thin film contacted by Ag electrodes. Although the measured value of the ensemble film is lower with respect to that obtained from photodetectors based on individual MoS_2 nanosheets [253], it is comparable to those based on graphene [254,255]. Ref. [41] demonstrated an all inkjet-printed photodetector with interdigitated graphene electrodes and a MoS_2 channel, observing a tenfold increase of conductance compared to dark conditions, suggesting the viable use of such devices as low-end photodetectors. Recently, printed graphene/WS_2 and CVD-grown graphene/WS_2 heterostructures have been used as photodetectors on SiO_2 and PET substrates achieving a photorespontivity ~1 mA W^{-1} [176].

An inkjet printed array of graphene and WS_2 heterostructures is shown to operate as a 4-bit passive read only memory (ROM) on Si/SiO_2 substrate [176]. No active devices are involved here (and is thus not not rewriteable) as the memory is fabricated at the time of printing. A junction between the graphene word line and the graphene bit line stores the logic '1' while a logic '0' is encoded by including a semiconducting layer (i.e. WS_2 in this case) between the graphene word line and bit line. It remains unclear what is the actual role of the graphene and the WS_2 printed patterns in the device operation and how this compares with other printed passive ROMs reported in literature.

Table 2
Printed electronics with pristine graphene.

Year	Process	Ink	Substrate	Printing Temperature	Annealing	Application	Ref.
2017	Inkjet	Graphene powder in ethanol &LPE graphene in water/sodium deoxycholate	Si/SiO_2	Room Temp	80 °C for 2 h	Terahertz saturable absorbers	[14]
2012	Inkjet	LPE graphene in NMP	Si/SiO_2 and glass with HMDS and O_2 treatment	n/a	170 °C for 5 min	TFT $\mu \sim 95\ cm^2\ V^{-1}\ s^{-1}$ ON/OFF ~ 10	[88]
2011	Inkjet	Electrochemically Synthesized graphene – PEDOT:PSS	Carbon Electrode	n/a	n/a	Electrochemical Sensor for salbutamol (SAL) – detection limit ~ 1.25 μM (3 S/N)	[277]
2013	Inkjet	LPE graphene in ethanol/ethyl cellulose redispersed in 85:15 cyclohexanone/terpineol	Kapton and HMDS-treated SiO_2	30 °C	250 °C for 30 min	Flexible electrodes $\sigma \approx 2.5 \times 10^4$ S/m	[126]
2013	Inkjet	LPE graphene in DMF/ethyl cellulose, solvent exchanged to terpineol/ethanol (3:1)	Glass slides, Si/SiO_2, Kapton	40 °C	375–400 °C for 30-60 min	TFT: $\mu \approx 0.12\ cm^2\ V^{-1}\ s^{-1}$ ON/OFF = 1.25 TCF: T ~ 80% Rs ≈ 30 kΩ/□ Micro-Supercapacitors: 0.59 mF cm^{-2}	[89]
2014	Inkjet	Expanded graphene with Ethylene glycol and Plasdone S-630	FS3 paper and LumiForte paper	50 °C	n/a	Conductive films on paper Rs ≈ 1–2 kΩ/□ Thickness = 800 nm	[105]
2014	Inkjet	LPE graphene mixed with ethyl cellulose and cyclohexanone	HDMS treated glass slides, PET and polyimide	n/a	300 °C for 30 min	Flexible Electrodes Rs ≈ 0.81 ± 0.2 kΩ/□ $T \approx 60\%$	[206]
2013	Inkjet	LPE graphene in water/SDBS, addition of polyaniline	Carbon fabric	Room Temp	80 °C for 2 h	Supercapacitors electrodes: Max Specific Cap ≈ 82 F g^{-1} Power density ≈ 124 kW kg^{-1} Energy density ≈ 2.4 W h kg^{-1}	[278]
2015	Inkjet	LPE graphene in water/EtOH	PET	n/a	None	Conductive stripes Rs ≈ 13 kΩ/□ $T = 22\%$	[159]
2015	Inkjet	LPE graphene in IPA/PVA	Metal interdigitated sensing electrodes on Si/SiO_2	n/a	400 °C for 30 min	CMOS devices as resistive humidity sensors	[279]
2015	Inkjet	High Shear mixing Graphene/ethyl cellulose in cyclohexanone/terpineol mixture (85:15)	PET, PEN, PI and glass	35 °C	200–300 °C	TCF for flexible electronics $\sigma \approx 2.5 \times 10^4$ S/m	[222]
2014	Inkjet	Graphene powder/ethyl cellulose in cyclohexanone-terpineol (85:15), addition of silver/organic complex (1:10)	Polyimide	n/a	300 °C for 40 min	Conductive flexible films Rs ≈ 17.4 kΩ/□ $\sigma \approx 2.16 \times 10^3$ S/m	[280]
2016	Inkjet	High shear mixing Graphene ethanol, DMF and NMP inks	Glass and PET	n/a	250 °C for 60 min	TCFs: Rs ≈ 260 Ω/□ $T = 86\%$ $\sigma \approx 4 \times 10^4$ S/m	[281]
2014	Inkjet	Graphene/PEDOT:PSS/ triton x-100 in dimethyl sulfoxide with ethylene glycol	Polymer substrate	n/a	n/a	Gas sensor for ammonia detection selectivity to NH_3 and response at 25-1000 ppm	[282]
2015	Inkjet	Graphene, deionized water ethylene glycol (60:40)	Si/SiO_2, Treated Si/SiO_2 and glass slides	Room Temp	160–200 °C for 2 h	Conductive Circuits	[283]
2016	Inkjet	Graphene powder/NMP mixed with PANI/NMP	Carbon electrode	n/a	120 °C for 5 min	Electrochemical Sensor for polyphenolic anti-oxidants	[284]
2015	Inkjet	LPE Graphene/MWCNT in water, ethanol, isopropanol, Dimethylformamide, ethylene glycol and their mixtures	paper	n/a	None	Conductive flexible films Rs ≈ 25 Ω/□ $\sigma \approx 1.4 \times 10^4$ S/m	[285]
2015	Inkjet	Graphene powder/MWCNT/ poly(acrylonitrile) in DMF	Photo paper	n/a	n/a	Conductive flexible films Rs ≈ 10^5 Ω/□	[286]
2017	Inkjet	LPE graphene powder/NMP mixed with PANI/NMP	Carbon electrode	30 °C	65 °C for 30 min	Electrochemical biosensor for human papillomavirus (HPV), Detection limit 2.3 nM	[287]

Table 2 (*Continued*)

Year	Process	Ink	Substrate	Printing Temperature	Annealing	Application	Ref.
2017	Inkjet	High shear mixing of Bromine intercalated graphene/Hydroxypropyl methyl cellulose in water	Glass and PET	n/a	100 °C for 60 min	Conductive flexible films $\sigma \approx 1 \times 10^5$ S/m	[288]
2016	Inkjet	LPE Graphene/pvp in IPA	Fluorine-doped SnO_2/glass	60 °C	400 °C for 30 min	Counter electrodes for DSSC ~3.0% conversion efficiency	[289]
2016	Inkjet	LPE graphene in Ethanol/ethyl cellulose	Si/SiO_2	Combustion anneal 300 °C for 15 min for each layer	300 °C for 45 min	Graphene Electrodes for TFT	[290]
2016	Inkjet	Graphene powder/ethyl cellulose in 80:15:5 v/v cyclohexanone, terpineol, and di(ethylene glycol) methyl ether	Polyimide	n/a	350 °C for 4 h	Graphene microsupercapacitors	[291]
2012	Inkjet	Electrochemical exfoliated graphene/PEDOT:PSS	Carbon Electrode	n/a	n/a	Biochemical Sensing of hydrogen peroxide, nicotinamide adenine dinucleotide and ferri/ferro cyanide	[292]
2013	Inkjet	Graphene/SDS/ ammonia	Polyimide	n/a	70 °C for 3 min followed by 400 °C for 3 h	Conductive flexible films $\sigma \approx 121.95$ S/m	[293]
2014	Flexo	Graphene powder/ Carboxymethylcellulose in water/isopropanol solution (7:1.5) and Graphene powder/NMP	PET	n/a	80 °C for 10 min	Dye sensitized solar cell electrode PCE = 2% FF = 66% Jsc = 4.1 mA cm^{-2} Voc = 730 mV	[174]
2015	Flexo & rod coating	Graphene powder/Platnium nanoparticles Carboxymethylcellulose in water/isopropanol solution (7:1.5)	PET	n/a	80 °C for 10 min	Dye sensitized solar cell electrode PCE = 4.6% FF = 67% Jsc = 10.01 mA cm^{-2} Voc = 690 mV	[294]
2014	Gravure	LPE graphene/ethyl cellulose in ethanol solvent exchanged to terpineol	Polyimide	70 °C	250 °C for 30 min	Conductive flexible films $\sigma \approx 1 \times 10^4$ S/m	[173]
2013	Screen	NGP/PANI hybrid inks + PTFE/water	PET and carbon fabric substrates	n/a	n/a	Supercapacitor Specific Cap: 26.8-352 F g^{-1} Power density: 454 kW kg^{-1} Energy density: 9.3 W h kg^{-1}	[79]
2015	Screen	LPE graphene/ethyl cellulose in toluene/ethanol (80:20)	Polyimide	n/a	300 °C for 30 min	Electrodes for electrolyte gated transistors $\sigma \approx 1.8 \times 10^4$ S/m	[90]
2015	Screen	LPE graphene in Ethyl Cellulose in Terpineol/ethanol	Glassine paper	n/a	Photonic annealing 2 pulses (1.66 J cm^{-2})	Electrodes for TFT $\sigma \approx 2.4 \times 10^3$ S/m	[295]
2012	Screen	LPE Graphene powder in IPA and Stoddard solvent (30:70) with PDMS + crosslinker (1:10)	PDMS	n/a	80 °C	Strain Gauge Strain operation (up to 40%) Gauge factor (>100)	[293]
2013	Screen	Graphene powder/ethyl cellulose/TiO_2/op emulsifier/acetylacetone in Terpinol	Fluorine doped Tin Oxide Glass	80 °C for 10 min for each layer	450 °C for 30 min	Dye sensitized solar cell electrode PCE = 6.49% FF = 0.692 Jsc = 13.7 mA cm^{-2} Voc = 685 mV	[296]
2015	Screen	Electrolytic exfoliation graphene/Sodium dodecylbenzenesulfonate (SDBS)/polyaniline nanofiber/acetylene black/polyteraflouroethylene in NMP, ethylene glycol and water (3.5:1.5:5)	Stainless Steel	n/a	80 °C for 5 h	Supercapacitor electrodes Specific capacitances: 690 F g^{-1} Power density: 454 kW kg^{-1} Energy density: 9.3 W h kg^{-1}	[297]
2013	Screen	Ru(bpy)/poly(sodium 4-styrenesulfonate) functionalized graphene powder and poly(ethylenimine) (BPEI)-functionalized graphene powder in tetrahydrofuran	Paper based chips	n/a	IR lamp for 180 s	Electrochemiluminescence (ECL) sensors For tripropylamine and tetracycline hydrochloride, detection limit 2.2 nM or detection limit 5 nM (S/N = 3)	[298]

Table 2 (*Continued*)

Year	Process	Ink	Substrate	Printing Temperature	Annealing	Application	Ref.
2016	Screen	Commerical graphene ink	Paper	n/a	100 °C for 10 min	Dipole Antenna Maximum Gain – 4 dBi at 870 MHz Bandwidth 984-105 MHz Radiation Efficiency – 32%	[299]
2015	Screen	High Shear Mixing of Intercalated Graphene and n-vinyl-2-pyrrolidone/vinyl acetate (60:40) in IPA	PET and Paper	n/a	100 °C for 5 min	Conductive flexible films $\sigma \approx 1.33 \times 10^3$ S/m	[300]
2012	Screen	Sonication of Intercalated Graphene in water	Polyimide	n/a	n/a	Flexible Electro-heating elements 172.3 °C at a driving voltage of 14 V.	[301]
2016	Screen	Commercial graphene/nonionic polymer-type surfactant in NMP	Paper	n/a	100 °C for 10 min	Antenna Bandwidth – 3.75 to 12.88 GHz Maximum Gain - 1.9 dBi at 10.06 GHz	[302]
2013	Screen	Ball Milling of graphene powder/ethyl cellulose in terpineol/ethanol	Fluorine doped Tin Oxide Glass	50 °C	n/a	Dye sensitized solar cell electrode PCE = 6.27% FF = 0.71 Jsc = 12.7 mA cm^{-2} Voc = 635 mV	[303]
2014	Screen	Sonication of graphene powder in PMMA/diethylene glycol butyl ether acetate	Paper and textile	n/a	130 °C for 30 min	Electrode in electroluminescent display T ≈ 70% Rs ≈ 10 kΩ/□	[304]
2014	Screen	Sonication of Graphene powder/aliphatic urethane acrylate/photoinitiator in water	Cotton fabric	n/a	IR lamp for 30 min	Gas Sensor: Methanol, Nitrogen and Acetone – 20% resistance sensitivity	[305]
2013	Screen	Intercalated graphene/ PANI/PSS in water	Paper	n/a	n/a	Flexible Antenna Bandwidth – 28.7 MHz	[306]
2015	Spray	LPE graphene/pvp in IPA	Paper	n/a	n/a	Electrode of Electroluminescent Device	[307]
2014	Spray	LPE graphene in 1,2-Dichlorobenzene followed by tip sonication	Polyurethane	250 °C	400 °C for 12 h	Biomedical conductive scaffold	[308]
2014	Spray & Screen	Graphene powder/PMMA in butyl carbitol acetate	PET	n/a	400 °C for 12 h	Screen Printed Conductive films T = 15% $\sigma \approx 1.5$ S/m Sprayed Conductive films T = 28.75% $\sigma \approx 26$ S/m	[309]
2015	Spray	Electrochemically exfoliated graphene/PEDOT:PSS in DMF	PET and SiO_2	90 °C	n/a	Flexible Conductive films $\sigma \approx 1000$ S/m T = 80% Transparent electrode for photodetector Responsivity ~ 0.16 AW^{-1} Photocurrent ~ 35 μA	[192]
2013	Spray	Sonicated graphene powder in IPA	Fluorine doped Tin Oxide Glass	n/a	300 °C for 30 min in N_2	Dye sensitized solar cell electrode PCE = 9.05% FF = 74% Jsc = 13.83 mA cm^{-2} Voc = 883 mV	[310]
2014	Spray	Ball milled graphene (functionalised) in water	Hanji (fibrous paper)	n/a	50 °C overnight	Flame Retardant	[311]
2014	Spray	Graphene powder in DMF	Stainless Steel	160 °C	160 °C	Li-ion battery Capacitance ≈100 mA h g^{-1}	[312]
2014	Spray	Commercial graphene/polymer in diethylene glycol and ethanol	poly(vinylidene difluoride)	60 °C	65 °C for 15 min, twice	Flexible and transparent touch panel electrodes: 44.6 ± 4.1 pC/N	[313]
2016	Spray	LPE graphene in DMF	Fluorine doped tin oxide glass	100 °C	400 °C for 60 min	Dye sensitized solar cell electrode T = 44% PCE = 3.5%	[314]
2018	Spray	LPE graphene/PDOT:PSS in ethanol &graphene nanoplatlets in ethanol	PMMA, PET and Si/SiO_2	20 °C	none	TCF for capacitive touch device $\sigma \approx 1 \times 10^4$ S/m $T \approx 65\%$	[154]

Table 3
Printed electronics with other 2D materials such as MoS_2, WS_2 and h-BN.

Year	Process	Ink	Substrate	Printing Temperature	Annealing	Application	Ref.
2017	Inkjet	LPE of graphene in NMP, solvent exchanged to ethanol, Microfluidization of h-BN in carboxymethylcellulose sodium salt/water	Polyester coated with polyurethane, PET coated with silica nanoparticles	Room temp	100 °C for 1 h	Fully printed graphene TFTs which are dielectrically gated with h-BN $\mu \approx 150\,cm^2\,V^{-1}\,s^{-1}$ $\mu_{max} \approx 204\,cm^2\,V^{-1}\,s^{-1}$ On/off ≈2.5 2 year stability 20 washing cycles Reprogrammable volatile memory cells Complementary inverters, OR logic gates Integrated circuits	[32]
2016	Inkjet	Graphene, MoS_2 in (IPA), Cyclohexanone/Terpineol (7:3) and NMP.	Polyimide and PET	n/a	300 °C for 1 h	Printed Graphene and MoS_2 Photodetector	[315]
2014	Inkjet	LPE MoS_2 powder in DMF + ethyl cellulose in 80:20 toluene:ethanol	Si/SiO_2	40 °C	160 °C for 20 min 450 °C for 1 h	MoS_2 Photodetector Responsivity ~ 36 μA W^{-1} Photocurrent ~57 pA	[252]
2017	Inkjet	Graphene, MoS_2, WS_2 and h-BN stabilised with pyrene/triton x-100 in water/propylene glycol (10:1) solvents	Si/SiO_2, q uartz, polyimide and PET (PEL P60 paper)	50 °C	300 °C for 1 h (for Si/SiO_2, quartz and polyimide)	WS_2 Photodetector Responsivity ~ 1 mA W^{-1}	[176]
2014	Inkjet	LPE graphene, h-BN, WS_2, MoS_2 NMP and DMF inks	PET Si/SiO_2	n/a	150 °C	WS_2 Photodetector Responsivity ~ 0.1 mA W^{-1}	[46]
2014	Inkjet	LPE MoS2 in NMP	PET coated with aluminium oxide and poly(vinyl alcohol)	60 °C	200 °C for 2 h under vacuum	Printed photodetectors with MoS_2 channel and graphene Electrodes Responsivity ~ 500 nAW^{-1} Photocurrent ~ 30 nA	[41]
2016	Inkjet & Spray	LPE graphene in NMP and h-BN in IPA	PET coated with aluminium oxide	n/a	n/a	Capacitors consisting of stacked heterostructures of graphene/boron-nitride/graphene 0.24 to 1.1 nF/cm^2	[175]
2013	Inkjet	MoS_2 in NMP transferred to ethanol/water mixture and sonicated, Glycerol then added to ink at 1:3 ratio	Si/SiO_2	60 °C	80 °C	NH_3 gas sensor	[316]
2017	Inkjet & Spray	WSe_2, WS_2, MoS_2, $MoSe_2$, h-BN and graphene powder in NMP solvent exchanged to IPA	Alumina coated PET	n/a	70 °C for 12 h	Electrolytic gated transistors On/Off ≈ 600 $\mu \approx 0.1\,cm^2\,V^{-1}\,s^{-1}$ $g_m \approx 5$ mS Electrolytic gated transistors with BN separator On/off ≈ 25 $g_m \approx 22$ μS	[256]
2015	Gravure	MoS_2/rGO	Polyimide	n/a	110 °C for 1 h	Flexible Micro-Supercapacitors Specific capacitance: 6.56 mF/cm^2 Energy Density: 0.583 mW h cm^{-3} Power Density: 13.4 mW h cm^{-3}	[317]
2016	Screen	h-BN powder/ Polycarbonate in DMF	Copper foil	n/a	50, 100, and 150 °C for 1 h	Copper-hBN-Silver Capacitor: ~80 pF/cm^2	[318]
2014	Spray	Molybdenum disulphide (MoS_2) powder/polyurethane in acetone and ethyl acetate	stainless steel, glass, fabric, and paper	n/a	120 °C for 2 h	Superhydrophobic coating for textiles: Water contact angle $\theta_c \approx 157°$	[193]
2017	Spray	LPE of h-BN in IPA	CVD graphene	n/a	400 °C for 30 min	Ultraviolet cathodoluminescent device	[319]

Despite several attempts to demonstrate fully-printed electronic devices based on 2D material heterostructures, the evidence of active devices, such as dielectrically gated transistors, exploiting the field effect for the channel modulation and consequently all-printed integrated circuits, was still missing until very recently.

While Refs. [176,175] demonstrated passive devices, there has been only one recent attempt to demonstrate current modulation in 2D crystal printed thin films [256], where a porous (60%) spray-coated h-BN layer is used as an electrochemical separator between the active layer from the evaporated gold top gate electrode. This was done using electrochemical gating by ionic liquid rather than by heterostructure-based dielectric gating, thus requiring ultra-high vacuum and low temperature (<100 K) to prevent water uptake into the electrolyte (which would damage the device). However, this does not represent a traditional FET structure given that no field effect is present across the gate dielectric, due to the absence of a dielectric layer.

The first fully inkjet printed dielectrically gated (h-BN) TFT structures (i.e inkjet printed source, drain, gate, channel and dielectric) have only recently been achieved [32] on both flexible (Fig. 9a) and textile substartes (Fig. 9b) which can be operated at both room temperature and pressure and at low operating voltages (<5 V) [32]. The graphene transistors had an average mobility of $\mu \approx 150\,cm^2\,V^{-1}\,s^{-1}$ and up to $\mu_{max} \approx 204\,cm^2\,V^{-1}\,s^{-1}$ on PET and

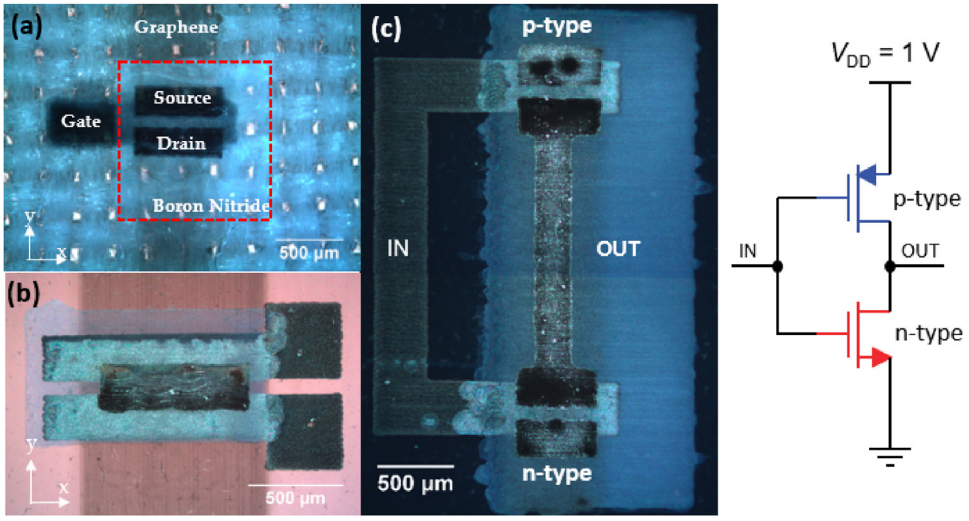

Fig. 9. FET heterostructure of Graphene/h-BN on PET (a) and textile (b). Optical microscopy (dark field) of an integrated circuit demonstrating an all inkjet-printed complementary graphene inverter as shown in the schematic. Adapted from Ref. [32] with permission.

$\mu \approx 91\ cm^2\ V^{-1}\ s^{-1}$ on polyester fabric [32]. The devices maintained their performance even under ~4% strain and showed stable operation for periods up to 2 years, indicating the two-fold role of the h-BN layer as a flexible dielectric and encapsulant [32]. Moreover the wearable TFTs on polyester textile were washable for up to 20 washing cycles indicating their robustness in harsh environments. These printed TFT devices paved the way to the first demonstration of fully printed volatile memory cells [32] with solution processed 2D materials which are reprogrammable and rely on the field effect modulation of the printed heterostructures, rather than on the "digital" properties of inkjet printing (i.e. the presence or absence of printed material) to define a bit. Moreover Ref. [32] also demonstrates complementary inverters (Fig. 9c), and OR logic gates with graphene/h-BN FETs which demonstrate the viability of the devices for printed and textile integrated circuits [32].

4.3 Sensors and wearable devices

The biocompatibility of the active material is a key requirement in biological [257] and chemical [258] sensors for flexible and printed electronics, enabling fully wearable devices. For large area, low-end and cost-effective applications, such as electrochemical detection of analytes for food and environmental monitoring [259], or interconnections in paper based lab-on-chip systems, the use of GO and LPE graphene, etc. could be sufficient [260].

A few examples, Ref. [257] demonstrated an antenna for a wireless bacteria detection system on tooth enamel was proposed by Mannoor et al. [257] where graphene was printed onto bioresorbable silk. The resistance of the graphene film changes as the analyte of interest is adsorbed on its surface, demonstrating a detection limit down to a single bacterium. A flexible sensor for NO_2 and Cl_2 vapors detection, based on RGO flakes (prepared by GO reduction with ascorbic acid) was inkjet-printed by Dua et al. [202] on flexible PET substrate. The resulting film has shown high sensitivity to vapors (order of part per billion), $\sigma \sim 15\ S\ cm^{-1}$ and fewer defects compared to the RGO films obtained by hydrazine reduction [102,261].

Ref. [262] reported electrochemical H_2O_2 sensors fabricated using inkjet-printed TFTs from single and few layer GO-based inks (GO printed on treated PET and polyimide plastic substrate). More recently, Ren et al. [263] demonstrated graphene strain and motion sensors fabricated directly on cotton fabric (Fig. 10a) using RGO films printed and reduced by an environmentally-friendly hot-press stamping process [263]. The graphene cotton fabric shows withstands 10 washing cycles and shows $R_s \sim 900\ \Omega/\square$, increasing by 3.5 times after 400 bending cycles (Fig. 10b).

4.4 Energy devices

Despite a vast majority of the energy applications of 2D crystal-based inks do not require printing processes (as these are mostly deposited by drop casting or coating) several electrodes for energy devices have been produced by printing processes such as inkjet and flexographic printing [264,89,174]. Inkjet printed electrodes with lateral spatial resolution in the order of ~50 μm have been used in supercapacitors with power density of $\sim 2.19\ kW\ kg^{-1}$ [264]. Ref. [89] fabricated an inkjet-printed micro-supercapacitor in a planar (interdigitated) structure on Kapton, characterized by specific capacitance of $\sim 0.6\ mF\ cm^{-2}$ and frequency response time of ~ 13 ms. Silver MNPs were initially printed as current collectors and the graphene was printed on the fingers as the active electrode. Graphene nano platelets ink flexographically printed onto flexible ITO/PET substrates has been demonstrated to act as a semitransparent catalytic layer for the realization of DSSC electrodes [174]. However the DSSC showed lower performances with respect to the ones reached with platinum catalyst, possibly due to the high optical absorption of the GNP electrode. Spray coated graphene inks have been used for the realization of transparent electrodes in large-area DSSC module. However, the efficiency of 3.5% and the Fill Factor (FF) of ~39% when using graphene sheets at the counter electrode result lower than the efficiency of 6.3% and FF of 67.4% when using the replaced and widely used platinum. More Reciently, Ref. [265] has demonstrated h-BN and graphene textiles can be overlaid to design an all-textile-based capacitive heterostructure (shown in Fig. 11) with an effective capacitance ~26 $pF\ cm^{-2}$ and flexibility down to at least 1 cm bending radius.

4.5 Printed THz devices

The generation of ultra-short laser pulses in the THz frequency is expected to have applications in communication technologies [266], security and spectroscopy [267] and in investigation of light-matter interaction phenomena [268]. Quantum cascade lasers (QCLs) are compact and spectrally pure, solid state semiconductor sources which can be used for light generation at THz frequencies [269], but presently do not operate passively in the ultra-short

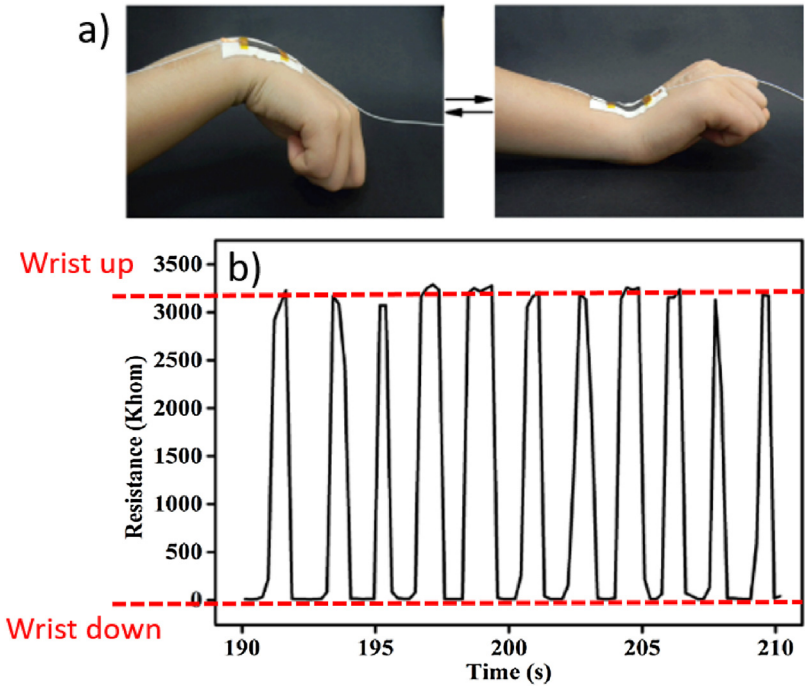

Fig. 10. (a) Graphene strain sensor fabricated directly on cotton fabric (b) The resistance of the strain sensor shows regular change in monitoring the wrist bending downwards and upwards, when in the "wrist up" state the resisantce is high, which decreases when in the "wrist down" state. Adapted from Ref. [263] with permission.

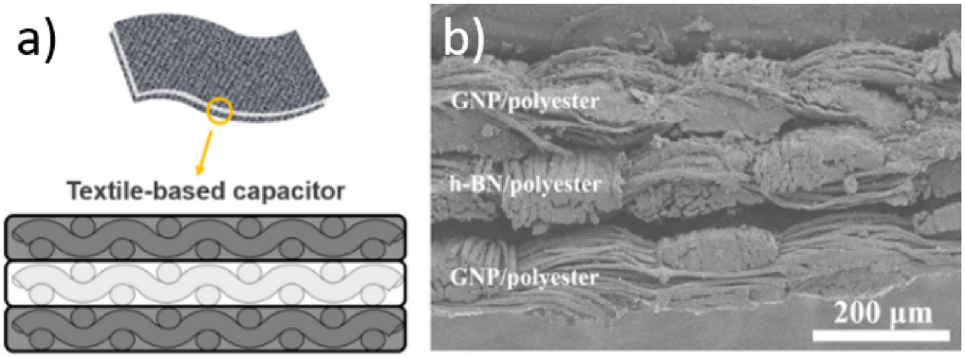

Fig. 11. (a) Schematic of the textile-based capacitor. (b) The cross-section SEM of h-BN/graphene capacitor showing the layered arrangement of the textile heterostructure. Adapted from Ref. [265] with permission.

pulse regime. Therefore, mode-locking strategies are required such as the use of a small and compact saturable absorbers (SA) which are routinely used to mode-lock lasers passively [270], enabling a train of short pulses to be derived from continuous wave operation. Semiconductors can be used as SAs over a wide frequency range (from the visible to the mid-infrared (MIR)) [271,272], however in the THz range, the photon energy (4–50 meV) is smaller than any semiconductor band-gap and the free-carrier absorption, α_{fr}, significantly increases as a function of wavelength [269]. Graphene [86,123] can overcome this issue, as broadband operation is intrinsic to graphene [86] and therefore has a unique application space in this field since suitable SAs in the THz region have previously not been available. Moreover graphene SAs have an ultrafast recovery time [273], low saturation fluence (the pulse energy density required to achieve saturation) [86], and are simple to fabricate [28] and integrate [260,274]. Graphene SAs have been demonstrated at frequencies from the visible to the IR [86,275], however only recently have they been shown to operate in the Thz regime [14]. In Ref. [14], graphene SAs are prepared with LPE inks and deposited by transfer coating and inkjet printing on Si/SiO_2 which show a transparency modulation up to ~80% [14]. The transparency modulation is almost one order of magnitude lager than graphene SAs prepared by CVD growth [276]. This highlights the benefits of solution processed graphene as the SAs have much higher absorption modulation and can be deposited, as required, on any substrate providing unprecedented compactness and resolution [14].

5 Outlook and future perspectives

Vast research efforts have been devoted to the exfoliation of layered crystals in suitable liquids yielding dispersions that can be further used for the formulation of functional inks, processed by established techniques such as spin and drop casting, spray coating, as well as inkjet, flexographic, gravure and screen printing. This strategy allows high versatility, reliability and mass production, as numerous bulk layered crystals can be exfoliated and processed in a similar way giving access to a broad range if tailored materials for a final application. The versatility of solution processed 2D crystals will also allow for some fine-tuning of electrochemical and optoelectronic properties by the addition of molecules or polymers that

provide supplementary functionalities as well as control on doping levels. But the most exciting applications of 2D materials in printed electronics will come from printing devices where two or more nanomaterials are integrated together in well-defined structures. The infinite possibilities offered by the printing and solution processing approach have enables exploiting the full potential of different conducting, semiconducting and dielectric 2D crystals for all-inkjet printed heterostructures, and it is likely that many developments will stem from these pioneering works.

However, printing processes based on 2D crystal inks are still at an early stage of development. Numerous challenges, from the first stage of the process chain toward devices produced from liquid-exfoliated 2D crystals, remain and need to be overcome in order to pave the way to industrially relevant processes or products in the end. Although liquid phase exfoliation of graphite has been explored over almost a decade, the extension of the same to other layered materials is still at its infancy. Moreover, the involved processes per se are still not well understood especially with regard to the emerging technologies such as shear or microfluidic exfoliation. In particular, it is very challenging to obtain accurate control over size and thickness of the flakes during the exfoliation, mainly because high throughput techniques to characterize length and thickness distributions have been lacking until very recently. This makes post-exfoliation size selection extremely important to match different requirements from various applications. Given the evolution of the electrical and optical properties of the flakes with the number of layers, ideally, dispersions consisting of monodisperse single and multi-layer crystal flakes will need to be made available. That means, flakes with the desired thickness are required having a well-defined size. Again, although significant progress has been made so far, still, the full achievement of this goal is far away from its practical realization. Furthermore, the production of large quantities of size selected samples, i.e., the increase in yield of both exfoliation and size selection, is a must.

A further challenge needs to be considered when transforming these dispersions in printable inks. The rheological properties of the ink need to be tailored on demand for the selected printing process. This means that parameters such as rheology, viscosities in both high- and low-boiling-point, which are not so crucial in the liquid phase exfoliation stage, become vital and will have to be controlled. We are currently far from the full achievement of this long list of requirements. One major problem in this regard is the fact that solvents that are good for exfoliation and nanosheet stabilization are not compatible with many printing processes. Hence, efficient ways to transfer the nanomaterial to any desired/targeted solvent, i.e., solvent exchange, at tailored concentration need to be further developed.

Heterostructure based advanced electronic and optoelectronic devices rely on the uniform, defect and impurity-free interface between the various layers. This is a major challenge in printed 2D crystal heterostructures due to the inherent poly-disperse (i.e. a combination of single-, multi-layer flakes) nature of the dispersed flakes, which ultimately offers a non-uniform interface. Moreover residual solvent and stabilizing agents may affect the interaction between the printed layers stack. This area is largely unexplored and it represents a focus of investigation for establishing the future of printed 2D crystal based heterostructures.

Last but not least, the issue with the scalability needs to be faced. In particular, to exploit the potential of 2D crystals in printed optoelectronics as well as energy storage and conversion, large quantities, i.e., tons, of exfoliated 2D crystals are needed. In this regard, despite the first demonstrations that these dispersions can be produced in industrially relevant quantities by the implementation of scalable exfoliation processes such as shear exfoliation or ball milling, further development and optimization are needed to assert their true potential. This work is part of a larger expanded work that can be found at ref. [320].

Acknowledgements

We acknowledge Mr Siyu Qiang for his useful input on the textile-based capacitor. The authors acknowledge funding from the EPSRC Grant EP/P02534X/1, ERC grant HETERO2D (319277), the Trinity College, Cambridge, and the Isaac Newton Trust.

References

[1] B.-J. de Gans, E. Kazancioglu, W. Meyer, U.S. Schubert, Macromol. Rapid Commun. 25 (1) (2004) 292–296.
[2] T.H.J. van Osch, J. Perelaer, A.W.M. de Laat, U.S. Schubert, Adv. Mater. 20 (2) (2008) 343.
[3] H. Sirringhaus, T. Kawase, R.H. Friend, T. Shimoda, M. Inbasekaran, W. Wu, E.P. Woo, Science 290 (5499) (2000) 2123–2126.
[4] K. Fukuda, Y. Takeda, M. Mizukami, D. Kumaki, S. Tokito, Sci. Rep. 4 (2014) 3947.
[5] E. Gili, M. Caironi, H. Sirringhaus, Appl. Phys. Lett. 100 (12) (2012) 123303.
[6] S. Park, R.S. Ruoff, Nat. Nanotechnol. 4 (2009) 217.
[7] S. Tekoglu, G. Hernandez-Sosa, E. Kluge, U. Lemmer, N. Mechau, Org. Electron. 14 (12) (2013) 3493–3499.
[8] K.-J. Baeg, M. Binda, D. Natali, M. Caironi, Y.-Y. Noh, Adv. Mater. 25 (31) (2013) 4267–4295.
[9] G. Azzellino, A. Grimoldi, M. Binda, M. Caironi, D. Natali, M. Sampietro, Adv. Mater. 25 (47) (2013) 6829–6833.
[10] M. Hosel, R.R. Sondergaard, D. Angmo, F.C. Krebs, Adv. Eng. Mater. 15 (10) (2013) 995–1001.
[11] F.C. Krebs, M. Jorgensen, K. Norrman, O. Hagemann, J. Alstrup, T.D. Nielsen, J. Fyenbo, K. Larsen, J. Kristensen, Sol. Energy Mater. Sol. Cells 93 (4) (2009) 422–441.
[12] Y. Noguchi, T. Sekitani, T. Someya, Appl. Phys. Lett. 89 (25) (2006) 253507.
[13] H.D. Goldberg, R.B. Brown, D.P. Liu, M.E. Meyerhoff, Sens. Actuators B: Chem. 21 (3) (1994) 171–183.
[14] V. Bianchi, T. Carey, L. Viti, L. Li, E.H. Linfield, A.G. Davies, A. Tredicucci, D. Yoon, P.G. Karagiannidis, L. Lombardi, F. Tomarchio, A.C. Ferrari, F. Torrisi, M.S. Vitiello, Nat. Commun. 8 (2017) 15763.
[15] C. Zhang, C.-L. Zou, Y. Zhao, C.-H. Dong, C. Wei, H. Wang, Y. Liu, G.-C. Guo, J. Yao, Y.S. Zhao, Sci. Adv. 1 (8) (2015).
[16] S. Gamerith, A. Klug, H. Scheiber, U. Scherf, E. Moderegger, E.J.W. List, Adv. Funct. Mater. 17 (16) (2007) 3111–3118.
[17] T. Takenobu, N. Miura, S.Y. Lu, H. Okimoto, T. Asano, M. Shiraishi, Y. Iwasa, Appl. Phys. Express 2 (2) (2009).
[18] H. Okimoto, T. Takenobu, K. Yanagi, Y. Miyata, H. Shimotani, H. Kataura, Y. Iwasa, Adv. Mater. 22 (36) (2010) 3981–3986.
[19] G.H. Gelinck, H.E.A. Huitema, E. van Veenendaal, E. Cantatore, L. Schrijnemakers, J.B.P.H. van der Putten, T.C.T. Geuns, M. Beenhakkers, J.B. Giesbers, B.-H. Huisman, E.J. Meijer, E.M. Benito, F.J. Touwslager, A.W. Marsman, B.J.E. van Rens, D.M. de Leeuw, Nat. Mater. 3 (2) (2004) 106–110.
[20] P. Servati, A. Nathan, Proc. IEEE 93 (7) (2005) 1257–1264.
[21] G. McKerricher, M. Vaseem, A. Shamim, Microsyst. Nanoeng. 3 (2017) 16075.
[22] R. Nagata, K. Yokoyama, S.A. Clark, I. Karube, Biosens. Bioelectron. 10 (3) (1995) 261–267.
[23] K. Ohfuji, N. Sato, N. Hamada-Sato, T. Kobayashi, C. Imada, H. Okuma, E. Watanabe, Biosens. Bioelectron. 19 (10) (2004) 1237–1244.
[24] H. Xin, L. Aâlei, H. Xuyang, S. Mingxia, D. Feng, L. Qiuming, X. Jundong, L. Junyan, Z. Mei, C. Yeqing, Z. Qingguang, Nanotechnology 27 (47) (2014) 475709.
[25] Y. Li, R. Torah, S. Beeby, J. Tudor, An all-inkjet printed flexible capacitor on a textile using a new poly(4-vinylphenol) dielectric ink for wearable applications, Proceedings of IEEE Sensors (2012) 13251299.
[26] J. Kang, Y. Jang, Y. Kim, S.-H. Cho, J. Suhr, B.H. Hong, J.-B. Choi, D. Byun, Nanoscale 7 (15) (2015) 6567–6573.
[27] C.N. Hoth, P. Schilinsky, S.A. Choulis, S. Balasubramanian, C.J. Brabec, Solution-processed organic photovoltaics, in: E. Cantatore (Ed.), Applications of Organic and Printed Electronics: A Technology-Enabled Revolution, Springer US, Boston, MA, 2012, pp. 27–56.
[28] F. Bonaccorso, A. Lombardo, T. Hasan, Z. Sun, L. Colombo, A.C. Ferrari, Mater. Today 15 (2012) 564–589.
[29] J.N. Coleman, M. Lotya, A. O'Neill, S.D. Bergin, P.J. King, U. Khan, K. Young, A. Gaucher, S. De, R.J. Smith, I.V. Shvets, S.K. Arora, G. Stanton, H.-Y. Kim, K. Lee, G.T. Kim, G.S. Duesberg, T. Hallam, J.J. Boland, J.J. Wang, J.F. Donegan, J.C. Grunlan, G. Moriarty, A. Shmeliov, R.J. Nicholls, J.M. Perkins, E.M. Grieveson, K. Theuwissen, D.W. McComb, P.D. Nellist, V. Nicolosi, Science (New York, N.Y.) 331 (2011) 568–571.
[30] F. Bonaccorso, A. Bartolotta, J.N. Coleman, C. Backes, Adv. Mater. 28 (29) (2016) 6136–6166.

[31] A.S. Mayorov, R.V. Gorbachev, S.V. Morozov, L. Britnell, R. Jalil, L.A. Ponomarenko, P. Blake, K.S. Novoselov, K. Watanabe, T. Taniguchi, A.K. Geim, Nano Lett. 11 (6) (2011) 2396–2399.
[32] T. Carey, S. Cacovich, G. Divitini, J. Ren, A. Mansouri, J.M. Kim, C. Wang, C. Ducati, R. Sordan, F. Torrisi, Nat. Commun. 8 (2017) 1202.
[33] Y.-M. Lin, C. Dimitrakopoulos, K.A. Jenkins, D.B. Farmer, H.-Y. Chiu, A. Grill, P. Avouris, Science 327 (5966) (2010) 662.
[34] F. Bonaccorso, Z. Sun, T. Hasan, A.C. Ferrari, Nat. Photonics 4 (9) (2010) 611–622.
[35] D.G. Purdie, D. Popa, V.J. Wittwer, Z. Jiang, G. Bonacchini, F. Torrisi, S. Milana, E. Lidorikis, A.C. Ferrari, Appl. Phys. Lett. 106 (2015) 253101.
[36] T.P. Call, T. Carey, P. Bombelli, D.J. Lea-Smith, P. Hooper, C.J. Howe, F. Torrisi, J. Mater. Chem. A 5 (45) (2017) 23872–23886.
[37] X. Xuan, M.F. Hossain, J.Y. Park, Sci. Rep. 6 (2016) 33125.
[38] X. Wang, P.F. Fulvio, G.A. Baker, G.M. Veith, R.R. Unocic, S.M. Mahurin, M. Chi, S. Dai, Chem. Commun. 46 (25) (2010) 4487–4489.
[39] K.R. Paton, E. Varrla, C. Backes, R.J. Smith, U. Khan, A. O'Neill, C. Boland, M. Lotya, O.M. Istrate, P. King, T. Higgins, S. Barwich, P. May, P. Puczkarski, I. Ahmed, M. Moebius, H. Pettersson, E. Long, J. Coelho, S.E. O'Brien, E.K. McGuire, B.M. Sanchez, G.S. Duesberg, N. McEvoy, T.J. Pennycook, C. Downing, A. Crossley, V. Nicolosi, J.N. Coleman, Nat. Mater. 13 (6) (2014) 624–630.
[40] P.G. Karagiannidis, S.A. Hodge, L. Lombardi, F. Tomarchio, N. Decorde, S. Milana, I. Goykhman, Y. Su, S.V. Mesite, D.N. Johnstone, R.K. Leary, P.A. Midgley, N.M. Pugno, F. Torrisi, A.C. Ferrari, ACS Nano 3 (11) (2017) 27422755.
[41] D. Finn, M. Lotya, G. Cunningham, R. Smith, D. McCloskey, J. Donegan, J.N. Coleman, J. Mater. Chem. C 2 (2014) 925–932.
[42] G. Wang, X. Shen, J. Yao, J. Park, Carbon 47 (8) (2009) 2049–2053.
[43] E. Kymakis, E. Stratakis, M.M. Stylianakis, E. Koudoumas, C. Fotakis, Thin Solid Films 520 (4) (2011) 1238–1241.
[44] X. Wang, L. Zhi, K. Müllen, Nano Lett. 8 (1) (2008) 323–327.
[45] X. Huang, T. Leng, X. Zhang, J.C. Chen, K.H. Chang, A.K. Geim, K.S. Novoselov, Z. Hu, Appl. Phys. Lett. 106 (20) (2015) 203105.
[46] F. Withers, H. Yang, L. Britnell, A.P. Rooney, E. Lewis, A. Felten, C.R. Woods, V. Sanchez Romaguera, T. Georgiou, A. Eckmann, Y.J. Kim, S.G. Yeates, S.J. Haigh, A.K. Geim, K.S. Novoselov, C. Casiraghi, Nano Lett. 14 (2014) 3922–3987.
[47] L.F. Mattheiss, Phys. Rev. B 8 (8) (1973) 3719–3740.
[48] J.A. Wilson, A.D. Yoffe, Adv. Phys. 18 (73) (1969) 193–335.
[49] Y. Hernandez, V. Nicolosi, M. Lotya, F.M. Blighe, Z. Sun, S. De, I.T. McGovern, B. Holland, M. Byrne, Y.K. Gun'Ko, J.J. Boland, P. Niraj, G. Duesberg, S. Krishnamurthy, R. Goodhue, J. Hutchison, V. Scardaci, A.C. Ferrari, J.N. Coleman, Nat. Nano 3 (2008) 563–568.
[50] M. Lotya, Y. Hernandez, P.J. King, R.J. Smith, V. Nicolosi, L.S. Karlsson, F.M. Blighe, S. De, W. Zhiming, I.T. McGovern, G.S. Duesberg, J.N. Coleman, J. Am. Chem. Soc. 131 (2009) 3611–3620.
[51] P. Jana, V.A. de la Pena O'Shea, J.M. Coronado, D.P. Serrano, Energy Environ. Sci. 4 (3) (2011) 778–783.
[52] A. Kamyshny, S. Magdassi, Small 10 (17) (2014) 3515–3535.
[53] F. Torrisi, J.N. Coleman, Nat. Nano 9 (10) (2014) 738–739.
[54] A.A. Tracton, Coatings Technology: Fundamentals, Testing, and Processing Techniques, CRC Press, 2006.
[55] X. Cheng, J.H. McCoy, J.N. Israelachvili, I. Cohen, Science (New York, N.Y.) 333 (6047) (2011) 1276–1279.
[56] F. Evans, H. Wennerström, The colloidal domain: where physics, chemistry, biology, and technology meet. By D. Fennell Evans and Hakån Wennerström. VCH Publishers, New York 1994, XXXII, 515 pp., hardcover, $65.00, DM 980, ISBN 1560815256, in: J.H. Fendler (Ed.), Advanced Materials, vol. 8, WILEY-VCH Verlag GmbH, Weinheim, 1996, p. 260.
[57] A. Lorenz, A. Senne, J. Rohde, S. Kroh, M. Wittenberg, K. Kraeger, F. Clement, D. Biro, Energy Procedia 67 (2015) 126–137.
[58] P.C. Hiemenz, Principles of colloid and surface chemistry, in: P.C. Hiemenz, R. Rajagopalan (Eds.), Fundamental and Applied Catalysis, CRC Press, New York, 1977.
[59] R.J. Good, Contact angle, wetting, and adhesion: a critical review, in: K.L. Mittal (Ed.), Contact Angle, Wettability and Adhesion, VSP, Utrecht, 1993.
[60] D. Myers, Surfaces, Interfaces, and Colloids: Principles and Applications, Wiley-VCH, Weinheim, 1999.
[61] E.G. Shafrin, W.A. Zisman, J. Phys. Chem. 64 (5) (1960) 519–524.
[62] P.G. de Gennes, Rev. Mod. Phys. 57 (3) (1985) 827.
[63] J. Israelachvili, Intermolecular and Surface Forces, Academic Press, 2011.
[64] T. Young, Philos. Trans. R. Soc. Lond. 95 (1805) 65–87.
[65] R.W. Bassemir, Surface phenomena in water-based flexo inks for printing on polyethylene films, in: F.J. Micale, M.K. Sharma (Eds.), Surface Phenomena and Fine Particles in Water-Based Coatings and Printing Technology, Plenum Press, New York, 1989.
[66] B. Derby, N. Reis, MRS Bull. 28 (11) (2003) 815–818.
[67] M. Singh, H.M. Haverinen, P. Dhagat, G.E. Jabbour, Adv. Mater. 22 (6) (2010) 673–685.
[68] G.K. Batchelor, J. Fluid Mech. 83 (1) (1977) 97–117.
[69] H. Dong, W.W. Carr, J.F. Morris, Phys. Fluids 18 (7) (2006).
[70] N. Reis, B. Derby, MRS Symp. Proc. 624 (2000) 65.
[71] D. Jang, D. Kim, J. Moon, Langmuir 25 (5) (2009) 2629–2635.
[72] J.E. Fromm, IBM J. Res. Dev. 28 (1984) 322.
[73] P. Shin, J. Sung, M.H. Lee, Microelectron. Reliab. 51 (4) (2011) 797–804.
[74] S. Jung, I.M. Hutchings, Soft Matter 8 (2012) 2686.
[75] W. Hsiao, S. Hoath, G. Martin, I. Hutchings, J. Imaging Sci. Technol. 53 (5) (2009) 050304.
[76] J. Perelaer, B.J. de Gans, U.S. Schubert, Adv. Mater. 18 (16) (2006) 2101–2104.
[77] D. Kim, S. Jeong, J. Moon, K. Kang, Mol. Cryst. Liquid Cryst. 459 (1) (2006) 45–55.
[78] D.S. Hecht, L. Hu, G. Irvin, Adv. Mater. 23 (13) (2011) 1482–1513.
[79] Y. Xu, M.G. Schwab, A.J. Strudwick, I. Hennig, X. Feng, Z. Wu, K. Müllen, Adv. Energy Mater. 3 (8) (2013) 1035–1040.
[80] V. Nicolosi, M. Chhowalla, M.G. Kanatzidis, M.S. Strano, J.N. Coleman, Science 340 (6139) (2013) 1226419.
[81] M. Osada, T. Sasaki, Adv. Mater. 24 (2) (2012) 209.
[82] M. Naguib, O. Mashtalir, J. Carle, V. Presser, J. Lu, L. Hultman, Y. Gogotsi, M.W. Barsoum, ACS Nano 6 (2) (2012) 1322–1331.
[83] J. Zhu, X. Liu, M.L. Geier, J.J. McMorrow, D. Jariwala, M.E. Beck, W. Huang, T.J. Marks, M.C. Hersam, Adv. Mater. 28 (1) (2015) 63–68.
[84] G. Abellan, C. Marta-Gastaldo, A. Ribera, E. Coronado, Acc. Chem. Res. 48 (6) (2015) 1601–1611.
[85] M. Chhowalla, H.S. Shin, G. Eda, L.-J. Li, K.P. Loh, H. Zhang, Nat. Chem. 5 (4) (2013) 263–275.
[86] Z. Sun, T. Hasan, F. Torrisi, D. Popa, G. Privitera, F. Wang, F. Bonaccorso, D.M. Basko, A.C. Ferrari, ACS Nano 4 (2) (2010) 803–810.
[87] F. Torrisi, D. Popa, S. Milana, Z. Jiang, T. Hasan, E. Lidorikis, A.C. Ferrari, Adv. Opt. Mater. 4 (7) (2016) 1088–1097.
[88] F. Torrisi, T. Hasan, W. Wu, Z. Sun, A. Lombardo, T.S. Kulmala, G.-W. Hsieh, S. Jung, F. Bonaccorso, P.J. Paul, D. Chu, A.C. Ferrari, ACS Nano 6 (4) (2012) 2992–3006.
[89] J. Li, F. Ye, S. Vaziri, M. Muhammed, M.C. Lemme, M. Åstling, Adv. Mater. 25 (29) (2013) 3985–3992.
[90] W.J. Hyun, E.B. Secor, M.C. Hersam, C.D. Frisbie, L.F. Francis, Adv. Mater. 27 (1) (2014) 109–115.
[91] K. Arapov, E. Rubingh, R. Abbel, J. Laven, G. de With, H. Friedrich, Adv. Funct. Mater. 26 (4) (2015) 586–593.
[92] J. Hassoun, F. Bonaccorso, M. Agostini, M. Angelucci, M.G. Betti, R. Cingolani, M. Gemmi, C. Mariani, S. Panero, V. Pellegrini, B. Scrosati, Nano Lett. 14 (8) (2014) 4901–4906.
[93] X. Wang, L. Zhi, K. Mullen, Nano Lett. 8 (1) (2007) 323–327.
[94] G. Eda, H.E. Unalan, N. Rupesinghe, G.A.J. Amaratunga, M. Chhowalla, Appl. Phys. Lett. 93 (23) (2008) 3.
[95] P. Blake, P.D. Brimicombe, R.R. Nair, T.J. Booth, D. Jiang, F. Schedin, L.A. Ponomarenko, S.V. Morozov, H.F. Gleeson, E.W. Hill, A.K. Geim, K.S. Novoselov, Nano Lett. 8 (6) (2008) 1704–1708.
[96] A. Penicaud, C. Drummond, Acc. Chem. Res. 46 (1) (2013) 129–137.
[97] P. Joensen, R.F. Frindt, S.R. Morrison, Mater. Res. Bull. 21 (4) (1986) 457–461.
[98] G.F. Walker, W.G. Garrett, Science 156 (3773) (1967) 385–387.
[99] S. Eigler, A. Hirsch, Angew. Chem. Int. Ed. 53 (30) (2014) 7720–7738.
[100] K. Parvez, Z.-S. Wu, R. Li, X. Liu, R. Graf, X. Feng, K. Mullen, J. Am. Chem. Soc. 16 (136) (2014) 6083–6091.
[101] M. Naguib, M. Kurtoglu, V. Presser, J. Lu, J. Niu, M. Heon, L. Hultman, Y. Gogotsi, M.W. Barsoum, Adv. Mater. 23 (37) (2014) 4248–4253.
[102] D.R. Dreyer, S. Park, C.W. Bielawski, R.S. Ruoff, Chem. Soc. Rev. 39 (1) (2010) 228–240.
[103] G. Eda, M. Chhowalla, Adv. Mater. 22 (22) (2010) 2392–2415.
[104] C. Mattevi, G. Eda, S. Agnoli, S. Miller, K.A. Mkhoyan, O. Celik, D. Mostrogiovanni, G. Granozzi, E. Garfunkel, M. Chhowalla, D. Mastrogiovanni, G. Granozzi, E. Garfunkel, M. Chhowalla, Adv. Funct. Mater. 19 (16) (2009) 2577–2583.
[105] K. Arapov, R. Abbel, G. de With, H. Friedrich, Faraday Discuss. 173 (2014) 323–336.
[106] S. Stankovich, D.A. Dikin, G.H.B. Dommett, K.M. Kohlhaas, E.J. Zimney, E.A. Stach, R.D. Piner, S.T. Nguyen, R.S. Ruoff, Nature 442 (7100) (2006) 282–286.
[107] T. Hasan, Z. Sun, F. Wang, F. Bonaccorso, P.H. Tan, A.G. Rozhin, A.C. Ferrari, Adv. Mater. 21 (38–39) (2009) 3874–3899.
[108] S.Z. Butler, S.M. Hollen, L. Cao, Y. Cui, J.A. Gupta, H.R. Gutiérrez, T.F. Heinz, S.S. Hong, J. Huang, A.F. Ismach, E. Johnston-Halperin, M. Kuno, V.V. Plashnitsa, R.D. Robinson, R.S. Ruoff, S. Salahuddin, J. Shan, L. Shi, M.G. Spencer, M. Terrones, W. Windl, J.E. Goldberger, ACS Nano 7 (4) (2013) 2898–2926.
[109] J.N. Coleman, Acc. Chem. Res. 46 (1) (2013) 14–22.
[110] A. Ciesielski, P. Samorì, Chem. Soc. Rev. 43 (1) (2014) 381–398.
[111] C. Backes, R.J. Smith, N. McEvoy, N.C. Berner, D. McCloskey, H.C. Nerl, A. O'Neill, P.J. King, T. Higgins, D. Hanlon, N. Scheuschner, J. Maultzsch, L. Houben, G.S. Duesberg, J.F. Donegan, V. Nicolosi, J.N. Coleman, Nat. Commun. 5 (2014) 4576.
[112] A.A. Green, M.C. Hersam, Nano Lett. 9 (12) (2009) 4031–4036.
[113] M. Lotya, P.J. King, U. Khan, S. De, J.N. Coleman, ACS Nano 4 (6) (2010) 3155–3162.
[114] H.M. Santos, C. Lodeiro, J.-L. Capelo-Martínez, Ultrasonic energy as a tool for sample treatment for the analysis of elements and elemental speciation, in: Ultrasound in Chemistry, Wiley-VCH Verlag GmbH & Co. KGaA, 2009, pp. 17–54.
[115] W. Zhao, M. Fang, F. Wu, H. Wu, L. Wang, G. Chen, J. Mater. Chem. 20 (28) (2010) 5817–5819.
[116] C. Knieke, A. Berger, M. Voigt, R.N.K. Taylor, J. Rohrl, W. Peukert, Carbon 48 (11) (2010) 3196–3204.
[117] Y. Yao, Z. Lin, Z. Li, X. Song, K.-S. Moon, C.-p. Wong, J. Mater. Chem. 22 (27) (2012) 13494–13499.
[118] L. Liu, Z. Shen, M. Yi, X. Zhang, S. Ma, RSC Adv. 4 (69) (2014) 36464–36470.

[119] J.S. Bunch, Y. Yaish, M. Brink, K. Bolotin, P.L. McEuen, Nano Lett. 5 (2) (2005) 287–290.
[120] T.J. Mason, Sonochemistry, Oxford University Press, 1999.
[121] M. Yi, Z. Shen, J. Mater. Chem. A 3 (22) (2015) 11700–11715.
[122] K. Kouroupis-Agalou, A. Liscio, E. Treossi, L. Ortolani, V. Morandi, N.M. Pugno, V. Palermo, Nanoscale 6 (11) (2014) 5926–5933.
[123] T. Hasan, F. Torrisi, Z. Sun, D. Popa, V. Nicolosi, G. Privitera, F. Bonaccorso, A.C. Ferrari, Phys. Status Solidi (B) Basic Res. 247 (11-12) (2010) 2953–2957.
[124] C.C. Nascentes, M. Korn, C.S. Sousa, M.A.Z. Arruda, J. Braz. Chem. Soc. 12 (2001) 57–63.
[125] M.M. Chivate, A.B. Pandit, Ultrason. Sonochem. 2 (1) (1995) S19–S25.
[126] E.B. Secor, P.L. Prabhumirashi, K. Puntambekar, M.L. Geier, M.C. Hersam, J. Phys. Chem. Lett. (2013) 1347–1351.
[127] J.R. Brent, N. Savjani, E.A. Lewis, S.J. Haigh, D.J. Lewis, P. O'Brien, Chem. Commun. 50 (87) (2014) 13338–13341.
[128] D. Hanlon, C. Backes, T.M. Higgins, M. Hughes, A. O'Neill, P. King, N. McEvoy, G.S. Duesberg, B. Mendoza Sanchez, H. Pettersson, V. Nicolosi, J.N. Coleman, Chem. Mater. 26 (4) (2014) 1751–1763.
[129] A. Liscio, K. Kouroupis-Agalou, X.D. Betriu, A. Kovtun, E. Treossi, N.M. Pugno, G.D. Luca, L. Giorgini, V. Palermo, 2D Mater. 4 (2) (2017) 025017.
[130] M.V. Bracamonte, G.I. Lacconi, S.E. Urreta, L.E.F. Foa Torres, J. Phys. Chem. C 118 (28) (2014) 15455–15459.
[131] V. Leon, M. Quintana, M.A. Herrero, J.L.G. Fierro, A. de la Hoz, M. Prato, E. Vazquez, Chem. Commun. 47 (39) (2011) 10936–10938.
[132] A. Fabbro, D. Scaini, V. Léon, E. Vázquez, G. Cellot, G. Privitera, L. Lombardi, F. Torrisi, F. Tomarchio, F. Bonaccorso, S. Bosi, A.C. Ferrari, L. Ballerini, M. Prato, ACS Nano 10 (1) (2016) 615–623.
[133] C. Damm, T.J. Nacken, W. Peukert, Carbon 81 (2015) 284–294.
[134] T.J. Nacken, C. Damm, H. Xing, A. Rüger, W. Peukert, Nano Res. 8 (6) (2015) 1865–1881.
[135] M.A. Ibrahem, T.-w. Lan, J.K. Huang, Y.-Y. Chen, K.-H. Wei, L.-J. Li, C.W. Chu, RSC Adv. 3 (32) (2013) 13193–13202.
[136] E. Varrla, C. Backes, K.R. Paton, A. Harvey, Z. Gholamvand, J. McCauley, J.N. Coleman, Chem. Mater. 27 (3) (2015) 1129–1139.
[137] A.H. Woomer, T.W. Farnsworth, J. Hu, R.A. Wells, C.L. Donley, S.C. Warren, ACS Nano 9 (9) (2015) 8869–8884.
[138] K.E. Paul, W.S. Wong, S.E. Ready, R.A. Street, Appl. Phys. Lett. 83 (10) (2003) 2070–2072.
[139] S.M. Kresta, R.S. Brodkey, Turbulence in mixing applications, in: Handbook of Industrial Mixing, John Wiley & Sons, Inc., 2004, pp. 19–87.
[140] T. Panagiotou, S.V. Mesite, J.M. Bernard, K.J. Chomistek, R.J. Fisher, NSTI-Nanotech 1 (2008) 688.
[141] J.A. Boxall, C.A. Koh, E.D. Sloan, A.K. Sum, D.T. Wu, Langmuir 28 (1) (2012) 104–110.
[142] A.N. Kolmogorov, Akad Nauk SSSR 30 (1941) 299.
[143] T. Lajunen, K. Hisazumi, T. Kanazawa, H. Okada, Y. Seta, M. Yliperttula, A. Urtti, Y. Takashima, Eur. J. Pharm. Sci. 62 (2014) 23–32.
[144] J. Yang, D. Vak, N. Clark, J. Subbiah, W.W.H. Wong, D.J. Jones, S.E. Watkins, G. Wilson, Sol. Energy Mater. Sol. Cells 109 (2013) 47–55.
[145] F.J. Tlle, M. Fabritius, R. Mlhaupt, Adv. Funct. Mater. 22 (6) (2012) 1136–1144.
[146] J. Lyklema, Colloids Surf. A: Physicochem. Eng. Asp. 156 (1–3) (1999) 413–421.
[147] C. Zhi, Y. Bando, C. Tang, H. Kuwahara, D. Golberg, Adv. Mater. 21 (28) (2009) 2889–2893.
[148] A. Jawaid, D. Nepal, K. Park, M. Jespersen, A. Qualley, P. Mirau, L.F. Drummy, R.A. Vaia, Chem. Mater. 28 (1) (2016) 337–348.
[149] A. Harvey, C. Backes, Z. Gholamvand, D. Hanlon, D. McAteer, H.C. Nerl, E. McGuire, A. Seral-Ascaso, Q.M. Ramasse, N. McEvoy, S. Winters, N.C. Berner, D. McCloskey, J.F. Donegan, G.S. Duesberg, V. Nicolosi, J.N. Coleman, Chem. Mater. 27 (9) (2015) 3483–3493.
[150] H.M. Solomon, B.A. Burgess, G.L. Kennedy, R.E. Staples, Drug Chem. Toxicol. 18 (4) (1995) 271–293.
[151] G.L. Kennedy, Drug Chem. Toxicol. 9 (2) (1986) 147–170.
[152] A. O'Neill, U. Khan, P.N. Nirmalraj, J. Boland, J.N. Coleman, J. Phys. Chem. C 115 (13) (2011) 5422–5428.
[153] A. Liscio, K. Kouroupis-Agalou, A. Kovtun, E. Gebremedhn, M. ElGarah, W. Rekab, E. Orgiu, L. Giorgini, P. Samor, D. Beljonne, V. Palermo, ChemPlusChem 82 (3) (2016) 358–367.
[154] T. Carey, C. Jones, F. Le Moal, D. Deganello, F. Torrisi, ACS Appl. Mater. Interfaces 10 (23) (2018) 19948–19956.
[155] K.G. Zhou, N.N. Mao, H.X. Wang, Y. Peng, H.L. Zhang, Angew. Chem. Int. Ed. 50 (46) (2011) 10839–10842.
[156] U. Halim, C.R. Zheng, Y. Chen, Z. Lin, S. Jiang, R. Cheng, Y. Huang, X. Duan, Nat. Commun. 4 (2013) 2213.
[157] D. Tasis, K. Papagelis, P. Spiliopoulos, C. Galiotis, Mater. Lett. 94 (2013) 47–50.
[158] I.S. Khattab, F. Bandarkar, M.A.A. Fakhree, A. Jouyban, Korean J. Chem. Eng. 29 (6) (2012) 812–817.
[159] A. Capasso, A.E. Del Rio Castillo, H. Sun, A. Ansaldo, V. Pellegrini, F. Bonaccorso, Solid State Commun. 224 (2015) 53–63.
[160] O.M. Marago, F. Bonaccorso, R. Saija, G. Privitera, P.G. Gucciardi, M.A. Lati, G. Calogero, P.H. Jones, F. Borghese, P. Denti, V. Nicolosi, A.C. Ferrari, ACS Nano 4 (12) (2010) 7515–7523.
[161] J.-W.T. Seo, A.A. Green, A.L. Antaris, M.C. Hersam, J. Phys. Chem. Lett. 2 (9) (2011) 1004–1008.
[162] S. Paria, K.C. Khilar, Adv. Colloid Interface Sci. 110 (3) (2004) 75–95.
[163] W. Wenseleers, I.I. Vlasov, E. Goovaerts, E.D. Obraztsova, A.S. Lobach, A. Bouwen, Adv. Funct. Mater. 14 (11) (2004) 1105–1112.
[164] J. Kang, J.-W.T. Seo, D. Alducin, A. Ponce, M.J. Yacaman, M.C. Hersam, Nat. Commun. 5 (2014) 5478.
[165] H. Zecha, Acta Polym. 32 (9) (1981) 582.
[166] T. Svedberg, K.O. Pedersen, The Ultracentrifuge, Oxford University Press, 1940.
[167] M. Behrens, Hoppe-Seylers Z. Physiol. Chem. 258 (1) (1939) 27.
[168] J.W. Williams, K.E. Van Holde, R.L. Baldwin, H. Fujita, Chem. Rev. 58 (1958) 715–806.
[169] U. Khan, A. O'Neill, M. Lotya, S. De, J.N. Coleman, Small 6 (7) (2010) 864–871.
[170] A. O'Neill, U. Khan, J.N. Coleman, Chem. Mater. 24 (12) (2012) 2414–2421.
[171] A. Nathan, A. Ahnood, M.T. Cole, S. Lee, Y. Suzuki, P. Hiralal, F. Bonaccorso, T. Hasan, L. Garcia-Gancedo, A. Dyadyusha, S. Haque, P. Andrew, S. Hofmann, J. Moultrie, D. Chu, A.J. Flewitt, A.C. Ferrari, M.J. Kelly, J. Robertson, G.A.J. Amaratunga, W.I. Milne, Flexible electronics: the next ubiquitous platform, Proceedings of the IEEE vol. 100 (2012) 1486–1517.
[172] M. Krueger, S. Berg, D. Stone, E. Strelcov, D.A. Dikin, J. Kim, L.J. Cote, J. Huang, A. Kolmakov, ACS Nano 5 (12) (2011) 10047–10054.
[173] E.B. Secor, S. Lim, H. Zhang, C.D. Frisbie, L.F. Francis, M.C. Hersam, Adv. Mater. 26 (26) (2014) 4533–4538.
[174] J. Baker, D. Deganello, D.T. Gethin, T.M. Watson, Mater. Res. Innovations 18 (2) (2014) 86–90.
[175] A.G. Kelly, D. Finn, A. Harvey, T. Hallam, J.N. Coleman, Appl. Phys. Lett. 109 (2) (2016) 23107.
[176] D. McManus, S. Vranic, F. Withers, V. Sanchez-Romaguera, M. Macucci, H. Yang, R. Sorrentino, K. Parvez, S.-K. Son, G. Iannaccone, K. Kostarelos, G. Fiori, C. Casiraghi, Nat. Nanotechnol. 12 (2017).
[177] X. Pi, Q. Li, D. Li, D. Yang, Sol. Energy Mater. Sol. Cells 95 (10) (2011) 2941–2945.
[178] R. Plass, S. Pelet, J. Krueger, M. Grätzel, U. Bach, J. Phys. Chem. B 106 (31) (2002) 7578–7580.
[179] C.I. Yeo, J.H. Choi, J.B. Kim, J.C. Lee, Y.T. Lee, Opt. Mater. Express 4 (2) (2014) 346–351.
[180] J. He, T. Kunitake, A. Nakao, Chem. Mater. 15 (23) (2003) 4401–4406.
[181] H.-Z. Geng, K.K. Kim, K.P. So, Y.S. Lee, Y. Chang, Y.H. Lee, J. Am. Chem. Soc. 129 (25) (2007) 7758–7759.
[182] E. Artukovic, M. Kaempgen, D.S. Hecht, S. Roth, G. GrUner, Nano Lett. 5 (4) (2005) 757–760.
[183] X. Yang, W. Fu, W. Liu, J. Hong, Y. Cai, C. Jin, M. Xu, H. Wang, D. Yang, H. Chen, J. Mater. Chem. A 2 (21) (2014) 7727–7733.
[184] Z. Wu, K. Parvez, X. Feng, K. Mullen, Nat. Commun. 4 (2013) 2487.
[185] B. Wang, L. Jinzhang, M. Francesca, P. Matteo, M. Nunzio, W.H. John, Nanotechnology 27 (16) (2016) 165402.
[186] T.T. Tung, R. Karunagaran, D.N.H. Tran, B. Gao, S. Nag-Chowdhury, I. Pillin, M. Castro, J.-F. Feller, D. Losic, J. Mater. Chem. C 4 (16) (2016) 3422–3430.
[187] J. Wang, M. Liang, Y. Fang, T. Qiu, J. Zhang, L. Zhi, Adv. Mater. 24 (21) (2012) 2874–2878.
[188] S. Gilje, S. Han, M. Wang, K.L. Wang, R.B. Kaner, Nano Lett. 11 (7) (2007).
[189] V.H. Pham, T.V. Cuong, S.H. Hur, E.W. Shin, J.S. Kim, J.S. Chung, E.J. Kim, Carbon 48 (7) (2010) 1945–1951.
[190] M. Sawangphruk, P. Srimuk, P. Chiochan, A. Krittayavathananon, S. Luanwuthi, J. Limtrakul, Carbon 60 (2013) 109–116.
[191] V. Tjoa, J. Chua, S.S. Pramana, J. Wei, S.G. Mhaisalkar, N. Mathews, ACS Appl. Mater. Interfaces 4 (7) (2012) 3447–3452.
[192] Y. Liu, F. Wang, X. Wang, X. Wang, E. Flahaut, X. Liu, Y. Li, X. Wang, Y. Xu, Y. Shi, R. Zhang, Nat. Commun. 6 (2015) 8589.
[193] Y. Tang, J. Yang, L. Yin, B. Chen, H. Tang, C. Liu, C. Li, Colloids Surf. A: Physicochem. Eng. Asp. 459 (2014) 261–266.
[194] T. Carey, Two-Dimensional Material Inks and Composites for Printed Electronics and Energy (Ph.D. thesis), University of Cambridge, 2018.
[195] M. Qian, T. Feng, H. Ding, L. Lin, H. Li, Y. Chen, Z. Sun, Nanotechnology 20 (42) (2009) 425702.
[196] A.C. Arias, J.D. MacKenzie, I. McCulloch, J. Rivnay, A. Salleo, Chem. Rev. 110 (1) (2010) 3–24.
[197] C. Ruiz, E.M. Garcia-Frutos, G. Hennrich, B. Gomez-Lor, J. Phys. Chem. Lett. 3 (11) (2012) 1428–1436.
[198] N.A. Luechinger, E.K. Athanassiou, W.J. Stark, Nanotechnology 19 (44) (2008) 445201.
[199] B.K. Park, D. Kim, S. Jeong, J. Moon, J.S. Kim, Thin Solid Films 515 (19) (2007) 7706–7711.
[200] T. Sekitani, T. Yokota, U. Zschieschang, H. Klauk, S. Bauer, K. Takeuchi, M. Takamiya, T. Sakurai, T. Someya, Science 326 (5959) (2009) 1516–1519.
[201] A. Jorio, C. Fantini, M.A. Pimenta, D.A. Heller, M.S. Strano, M.S. Dresselhaus, Y. Oyama, J. Jiang, R. Saito, Appl. Phys. Lett. 88 (2) (2006).
[202] V. Dua, S. Surwade, S. Ammu, S. Agnihotra, S. Jain, K. Roberts, S. Park, R. Ruoff, S. Manohar, Angew. Chem. Int. Ed. 49 (12) (2010) 2154–2157.
[203] B. Derby, Annual Review of Materials Research 40 (1) (2010) 395–414.
[204] P. Calvert, Chem. Mater. 13 (10) (2001) 3299.
[205] A. Kamyshny, S. Magdassi, Inkjet ink formulations, in: Inkjet-Based Micromanufacturing, Wiley-VCH Verlag GmbH & Co. KGaA, 2012, pp. 173–189.
[206] Y. Gao, W. Shi, W. Wang, Y. Leng, Y. Zhao, Ind. Eng. Chem. Res. 53 (43) (2014) 16777–16784.
[207] J. Li, M.C. Lemme, M. Östling, ChemPhysChem 15 (16) (2014) 3427–3434.

[208] Y.H. Kim, B. Yoo, J.E. Anthony, S.K. Park, Adv. Mater. 24 (4) (2012) 497–502.
[209] S. Brimaud, C. Coutanceau, E. Garnier, J.M. Lager, F. Garard, S. Pronier, M. Leoni, J. Electroanal. Chem. 602 (2) (2007) 226–236.
[210] C. Backes, B.M. Szydłowska, A. Harvey, S. Yuan, V. Vega-Mayoral, B.R. Davies, P.-l. Zhao, D. Hanlon, E.J.G. Santos, M.I. Katsnelson, W.J. Blau, C. Gadermaier, J.N. Coleman, ACS Nano 10 (1) (2016) 1589–1601.
[211] G. Cunningham, M. Lotya, C.S. Cucinotta, S. Sanvito, S.D. Bergin, R. Menzel, M.S.P. Shaffer, J.N. Coleman, ACS Nano 6 (4) (2012) 3468–3480.
[212] R.J. Smith, P.J. King, M. Lotya, C. Wirtz, U. Khan, S. De, A. O'Neill, G.S. Duesberg, J.C. Grunlan, G. Moriarty, J. Chen, J. Wang, A.I. Minett, V. Nicolosi, J.N. Coleman, Adv. Mater. 23 (34) (2011) 3944–3948.
[213] V.G. Kravets, A.N. Grigorenko, R.R. Nair, P. Blake, S. Anissimova, K.S. Novoselov, A.K. Geim, Phys. Rev. B – Condens. Matter Mater. Phys. 81 (15) (2010).
[214] K.R. Paton, J.N. Coleman, Carbon 107 (2016) 733–738.
[215] A.C. Ferrari, J.C. Meyer, V. Scardaci, C. Casiraghi, M. Lazzeri, F. Mauri, S. Piscanec, D. Jiang, K.S. Novoselov, S. Roth, A.K. Geim, Phys. Rev. Lett. 97 (18) (2006).
[216] J.C. Meyer, A.K. Geim, M.I. Katsnelson, K.S. Novoselov, T.J. Booth, S. Roth, Nature 446 (7131) (2007) 60–63.
[217] K.S. Novoselov, D. Jiang, F. Schedin, T.J. Booth, V.V. Khotkevich, S.V. Morozov, A.K. Geim, Proc. Natl. Acad. Sci. U. S. A. 102 (30) (2005) 10451–10453.
[218] C. Valles, C. Drummond, H. Saadaoui, C.A. Furtado, M. He, O. Roubeau, L. Ortolani, M. Monthioux, A. Penicaud, J. Am. Chem. Soc. 130 (47) (2008) 15802.
[219] M. Dobbelin, A. Ciesielski, S. Haar, S. Osella, M. Bruna, A. Minoia, L. Grisanti, T. Mosciatti, F. Richard, E.A. Prasetyanto, L. De Cola, V. Palermo, R. Mazzaro, V. Morandi, R. Lazzaroni, A.C. Ferrari, D. Beljonne, P. Samorì, Nat. Commun. 7 (2016) 11090.
[220] J.F. Padday, Philos. Trans. R. Soc. Lond. A 269 (1971) 265–293.
[221] T.G. Mezger, The Rheology Handbook: for Users of Rotational and Oscillatory Rheometers, Vincentz, Hannover, 2006.
[222] E.B. Secor, B.Y. Ahn, T.Z. Gao, J.A. Lewis, M.C. Hersam, Adv. Mater. 27 (42) (2015) 6683–6688.
[223] A. Pekarovicova, V. Husovska, 3 – Printing ink formulations, in: Printing on Polymers, William Andrew Publishing, 2016, pp. 41–55.
[224] F.M. Smits, Measurements of Sheet Resistivity with the Four-Point Probe vol. 37 (1958).
[225] S. De, P.J. King, P.E. Lyons, U. Khan, J.N. Coleman, ACS Nano 4 (12) (2010) 7064–7072.
[226] S. De, P.E. Lyons, S. Sorel, E.M. Doherty, P.J. King, W.J. Blau, P.N. Nirmalraj, J.J. Boland, V. Scardaci, J. Joimel, J.N. Coleman, ACS Nano 3 (3) (2009) 714–720.
[227] C. Sire, F. Ardiaca, S. Lepilliet, J.-W.T. Seo, M.C. Hersam, G. Dambrine, H. Happy, V. Derycke, Nano Lett. 12 (3) (2011) 1184–1188.
[228] S. Ghosh, A. Winchester, B. Muchharla, M. Wasala, S. Feng, A.L. Elias, M.B.M. Krishna, T. Harada, C. Chin, K. Dani, S. Kar, M. Terrones, S. Talapatra, Sci. Rep. 5 (2015) 11272.
[229] R. Das, http://www.idtechex.com (accessed 2016).
[230] Y.Y. Noh, K.J. Baeg, Inkjet-printed electronic circuits based on organic semiconductors, in: M. Caironi, Y.Y. Noh (Eds.), Large Area and Flexible Electronics, Wiley, Amsterdam, 2014.
[231] B.S. Ong, Y. Wu, P. Liu, S. Gardner, J. Am. Chem. Soc. 126 (11) (2004) 3378–3379.
[232] A.C. Arias, S.E. Ready, R. Lujan, W.S. Wong, K.E. Paul, A. Salleo, M.L. Chabinyc, R. Apte, R.A. Street, Y. Wu, P. Liu, B. Ong, Appl. Phys. Lett. 85 (15) (2004) 3304–3306.
[233] Y. Wu, P. Liu, B.S. Ong, T. Srikumar, N. Zhao, G. Botton, S. Zhu, Appl. Phys. Lett. 86 (14) (2005) 142102–142103.
[234] K. Kaneto, M. Yano, M. Shibao, T. Morita, W. Takashima, J. Appl. Phys. 46 (2007) 1736–1738.
[235] T. Morita, V. Singh, S. Oku, S. Nagamatsu, W. Takashima, S. Hayase, K. Kaneto, J. Appl. Phys. 49 (2010) 4161–4166.
[236] P. Beecher, P. Servati, A. Rozhin, A. Colli, V. Scardaci, S. Pisana, T. Hasan, A.J. Flewitt, J. Robertson, G.W. Hsieh, F.M. Li, A. Nathan, A.C. Ferrari, W.I. Milne, J. Appl. Phys. 102 (4) (2007) 43710.
[237] G.W. Hsieh, F.M. Li, P. Beecher, A. Nathan, Y.L. Wu, B.S. Ong, W.I. Milne, J. Appl. Phys. 106 (12) (2009) 7.
[238] H. Okimoto, T. Takenobu, K. Yanagi, Y. Miyata, H. Kataura, T. Asano, Y. Iwasa, Jpn J. Appl. Phys. 48 (6) (2009) 4.
[239] M. Ha, Y. Xia, A.A. Green, W. Zhang, M.J. Renn, C.H. Kim, M.C. Hersam, C.D. Frisbie, ACS Nano 4 (8) (2010) 4388–4395.
[240] H. Sirringhaus, N. Tessler, R.H. Friend, Science 280 (5370) (1998) 1741–1744.
[241] Y.J. Song, J.U. Lee, W.H. Jo, Carbon 48 (2) (2010) 389–395.
[242] G.L. Whiting, A.C. Arias, Appl. Phys. Lett. 95 (25) (2009) 253302–253303.
[243] H. Klauk, Organic Electronics: Materials, Manufacturing, and Applications, Wiley-VCH Verlag GmbH & Co. KGaA, 2006.
[244] H. Sandberg, Polymer Field Effect transistors, in: S.S. Sun, L.R. Dalton (Eds.), Introduction to Organic Electronic and Optoelectronic Materials and Devices, Taylor & Francis, 2008.
[245] B. Radisavljevic, A. Radenovic, J. Brivio, V. Giacometti, A. Kis, B. Radisavljevic, A. Rade-novic, J. Brivio, V. Giacometti, A. Kis, Nat Nano 6 (3) (2011) 147–150.
[246] B. Radisavljevic, M.B. Whitwick, A. Kis, ACS Nano 5 (12) (2011) 9934–9938.
[247] A. Castellanos-Gomez, L. Vicarelli, E. Prada, J.O. Island, K.L. Narasimha-Acharya, I.B. Sofya, D.J.G. Groenendijk, M. Buscema, G.A. Steele, J.V. Alvarez, W.H. Zandbergen, J.J. Palacios, H. van der Zant, 2D Mater. 1 (2) (2014) 25001.
[248] A.J. Molina-Mendoza, E. Giovanelli, W.S. Paz, M.A. Niño, J.O. Island, C. Evangeli, L. Aballe, M. Foerster, H.S.J. van der Zant, G. Rubio-Bollinger, N. Agraït, J.J. Palacios, E.M. Parez, A. Castellanos-Gomez, Nat. Commun. 8 (2016) 14409.
[249] R.G. Gordon, Mater. Res. Bull. 25 (2000) 52.
[250] I. Hamberg, C.G. Granqvist, J. Appl. Phys. 60 (11) (1986) R123–R160.
[251] M.W. Rowell, M.D. McGehee, Energy Environ. Sci. 4 (1) (2011) 131–134.
[252] J. Li, M.M. Naiini, S. Vaziri, M.C. Lemme, M. Östling, Adv. Funct. Mater. 24 (2014) 6524.
[253] O. Lopez-Sanchez, D. Lembke, M. Kayci, A. Radenovic, A. Kis, Nat. Nanotechnol. 8 (7) (2013) 497–501.
[254] F. Xia, T. Mueller, Y.-m. Lin, A. Valdes-Garcia, P. Avouris, Nat Nano 4 (12) (2009) 839–843.
[255] M.C. Lemme, F.H.L. Koppens, A.L. Falk, M.S. Rudner, H. Park, L.S. Levitov, C.M. Marcus, Nano Lett. 11 (10) (2011) 4134–4137.
[256] A.G. Kelly, T. Hallam, C. Backes, A. Harvey, A.S. Esmaeily, I. Godwin, J. Coelho, V. Nicolosi, J. Lauth, A. Kulkarni, S. Kinge, L.D.A. Siebbeles, G.S. Duesberg, J.N. Coleman, Science 356 (6333) (2017) 69–73.
[257] M.S. Mannoor, H. Tao, J.D. Clayton, A. Sengupta, D.L. Kaplan, R.R. Naik, N. Verma, F.G. Omenetto, M.C. McAlpine, Nat. Commun. 3 (2012) 763.
[258] B. Mailly-Giacchetti, A. Hsu, H. Wang, V. Vinciguerra, F. Pappalardo, L. Occhipinti, E. Guidetti, S. Coffa, J. Kong, T. Palacios, J. Appl. Phys. 114 (8) (2013) 84505.
[259] G. Alarcon-Angeles, G.A. Álvarez-Romero, A. Merkoçi, Graphene and carbon nanotube-based electrochemical biosensors for environmental monitoring, in: Advanced Carbon Materials and Technology, John Wiley & Sons, Inc., 2013, pp. 87–128.
[260] A.C. Ferrari, M. Katsnelson, L. Vandersypen, A. Loiseau, V. Morandi, A. Tredicucci, G.M. Williams, H. Hong, Nanoscale 7 (11) (2015) 4598–4810.
[261] M.J. Allen, V.C. Tung, R.B. Kaner, Chem. Rev. 110 (1) (2010) 132–145.
[262] L. Huang, Y. Huang, J. Liang, X. Wan, Y. Chen, Nano Res. 4 (7) (2011) 675–684.
[263] J. Ren, C. Wang, X. Zhang, T. Carey, K. Chen, Y. Yin, F. Torrisi, Carbon 111 (2017) 622–630.
[264] L.T. Le, M.H. Ervin, H. Qiu, B.E. Fuchs, W.Y. Lee, Electrochem. Commun. 13 (4) (2011) 355–358.
[265] S. Qiang, T. Carey, A. Arbab, W. Song, C. Wang, F. Torrisi, submitted for publication, 2018.
[266] T. Shao, H. Shams, P.M. Anandarajah, M.J. Fice, C.C. Renaud, F. Van Dijk, A.J. Seeds, L.P. Barry, IEEE Trans. Terahertz Sci. Technol. 5 (4) (2015) 590–597.
[267] A. Korobenko, A.A. Milner, V. Milner, Phys. Rev. Lett. 112 (11) (2014).
[268] M. Eisele, T.L. Cocker, M.A. Huber, M. Plankl, L. Viti, D. Ercolani, L. Sorba, M.S. Vitiello, R. Huber, Nat. Photonics 8 (11) (2014) 841–845.
[269] M.S. Vitiello, G. Scalari, B. Williams, P.D. Natale, Opt. Express 23 (4) (2015) 5167–5182.
[270] U. Keller, Nature 424 (6950) (2003) 831–838.
[271] U. Keller, K.J. Weingarten, F.X. Kärtner, D. Kopf, B. Braun, I.D. Jung, R. Fluck, C. Hönninger, N. Matuschek, J. Aus Der Au, IEEE J. Sel. Top. Quantum Electron. 2 (3) (1996) 435–451.
[272] A.A. Lagatsky, F.M. Bain, C.T.A. Brown, W. Sibbett, D.A. Livshits, G. Erbert, E.U. Rafailov, Appl. Phys. Lett. 91 (23) (2007).
[273] D. Brida, A. Tomadin, C. Manzoni, Y.J. Kim, A. Lombardo, S. Milana, R.R. Nair, K.S. Novoselov, A.C. Ferrari, G. Cerullo, M. Polini, Nat. Commun. 4 (2013) 1–9.
[274] A. Tredicucci, M.S. Vitiello, IEEE J. Sel. Top. Quantum Electron. 20 (1) (2014).
[275] R. Mary, G. Brown, S. Beecher, F. Torrisi, Opt. Express 21 (7) (2013) 11.
[276] F. Bianco, V. Miseikis, D. Convertino, J.-H. Xu, F. Castellano, H.E. Beere, D.A. Ritchie, M.S. Vitiello, A. Tredicucci, C. Coletti, Opt. Express 23 (9) (2015) 11632.
[277] C. Karuwan, C. Sriprachuabwong, A. Wisitsoraat, D. Phokharatkul, P. Sritongkham, A. Tuantranont, Sens. Actuators B: Chem. 161 (1) (2012) 549–555.
[278] Y. Xu, I. Hennig, D. Freyberg, A. James Strudwick, M. Georg Schwab, T. Weitz, K. Chih-Pei Cha, J. Power Sources 248 (2014) 483–488.
[279] S. Santra, G. Hu, R.C.T. Howe, A. De Luca, S.Z. Ali, F. Udrea, J.W. Gardner, S.K. Ray, P.K. Guha, T. Hasan, Sci. Rep. 5 (2015) 17374.
[280] G. Wang, Z. Wang, Z. Liu, J. Xue, G. Xin, Q. Yu, J. Lian, M.Y. Chen, Chem. Eng. J. 260 (2015) 582–589.
[281] S. Majee, M. Song, S.-L. Zhang, Z.-B. Zhang, Carbon 102 (2016) 51–57.
[282] Y. Seekaew, S. Lokavee, D. Phokharatkul, A. Wisitsoraat, T. Kerdcharoen, C. Wongchoosuk, Org. Electron.: Phys. Mater. Appl. 15 (11) (2014) 2971–2981.
[283] S. Chen, M. Su, C. Zhang, M. Gao, B. Bao, Q. Yang, B. Su, Y. Song, Adv. Mater. 27 (26) (2015) 3928–3933.
[284] C. Bardpho, P. Rattanarat, W. Siangproh, O. Chailapakul, Talanta 148 (2016) 673–679.
[285] V. Georgakilas, A. Demeslis, E. Ntararas, A. Kouloumpis, K. Dimos, D. Gournis, M. Kocman, M. Otyepka, R. Zbořil, Adv. Funct. Mater. 25 (10) (2015) 1481–1487.
[286] W. Shim, Y. Kwon, S.-Y. Jeon, W.-R. Yu, Sci. Rep. 5 (2015) 16568.
[287] P. Teengam, W. Siangproh, A. Tuantranont, C.S. Henry, T. Vilaivan, O. Chailapakul, Anal. Chim. Acta 952 (2017) 32–40.
[288] S. Majee, C. Liu, B. Wu, S.L. Zhang, Z.B. Zhang, Carbon 114 (2017) 77–83.
[289] D. Dodoo-Arhin, R.C. Howe, G. Hu, Y. Zhang, P. Hiralal, A. Bello, G. Amaratunga, T. Hasan, Carbon 105 (2016) 33–41.
[290] E.B. Secor, J. Smith, T.J. Marks, M.C. Hersam, ACS Appl. Mater. Interfaces 8 (27) (2016) 17428–17434.
[291] L. Li, E.B. Secor, K.S. Chen, J. Zhu, X. Liu, T.Z. Gao, J.W.T. Seo, Y. Zhao, M.C. Hersam, Adv. Energy Mater. 6 (20) (2016) 1–8.

[292] C. Sriprachuabwong, C. Karuwan, A. Wisitsorrat, D. Phokharatkul, T. Lomas, P. Sritongkham, A. Tuantranont, J. Mater. Chem. 22 (12) (2012) 5478.
[293] C. Lee, L. Jug, E. Meng, Appl. Phys. Lett. 102 (18) (2013).
[294] J. Baker, J.D. McGettrick, D.T. Gethin, T.M. Watson, J. Electrochem. Soc. 162 (8) (2015) H564–H569.
[295] W.J. Hyun, E.B. Secor, G.A. Rojas, M.C. Hersam, L.F. Francis, C.D. Frisbie, Adv. Mater. 27 (44) (2015) 7058–7064.
[296] H. Zhang, W. Wang, H. Liu, R. Wang, Y. Chen, Z. Wang, Mater. Res. Bull. 49 (1) (2014) 126–131.
[297] J.P. Mensing, A. Wisitsoraat, D. Phokharatkul, T. Lomas, A. Tuantranont, Compos. Part B: Eng. 77 (2015) 93–99.
[298] W. Gu, Y. Xu, B. Lou, Z. Lyu, E. Wang, Electrochem. Commun. 38 (2014) 57–60.
[299] T. Leng, X. Huang, K. Chang, J. Chen, M.A. Abdalla, Z. Hu, IEEE Antennas Wireless Propag. Lett. 15 (2016) 1565–1568.
[300] K. Arapov, E. Rubingh, R. Abbel, J. Laven, G. De With, H. Friedrich, Adv. Funct. Mater. 26 (4) (2016) 586–593.
[301] K.-Y. Shin, J.-Y. Hong, S. Lee, J. Jang, J. Mater. Chem. 22 (44) (2012) 23404.
[302] X.H. Hu, T. Leng, K.H. Chang, J.C. Chen, K.S. Novoselov, Z.R. Hu, 2D Mater. 3 (2) (2016) 25021.
[303] Y. Rong, H. Han, J. Nanophotonics 7 (1) (2013) 73090.
[304] M. Sloma, D. Janczak, G. Wroblewski, A. Mlozniak, M. Jakubowska, Circuit World 40 (1) (2014) 13–16.
[305] E. Skrzetuska, M. Puchalski, I. Krucinska, Sensors (Switzerland) 14 (9) (2014) 16816–16828.
[306] K.Y. Shin, S. Cho, J. Jang, Small 9 (22) (2013) 3792–3798.
[307] R.C.T. Howe, G. Hu, Z. Yang, T. Hasan, Proc. SPIE 9553 (2015) 95530R.
[308] S. Meng, Tissue Eng. Regener. Med. 11 (4) (2014) 274–283.
[309] G. Wroblewski, M. S-loma, D. Janczak, A. Mlozniak, M. Jakubowska, Acta Phys. Pol. A 125 (4) (2014) 861–863.
[310] M.J. Ju, J.C. Kim, H.J. Choi, I.T. Choi, S.G. Kim, K. Lim, J. Ko, J.J. Lee, I.Y. Jeon, J.B. Baek, H.K. Kim, ACS Nano 7 (6) (2013) 5243–5250.
[311] M.J. Kim, I.Y. Jeon, J.M. Seo, L. Dai, J.B. Baek, ACS Nano 8 (3) (2014) 2820–2825.
[312] J.-H. Choi, W.-H. Ryu, K. Park, J.-D. Jo, S.-M. Jo, D.-S. Lim, I.-D. Kim, Sci. Rep. 4 (2014) 7334.
[313] T. Vuorinen, M. Zakrzewski, S. Rajala, D. Lupo, J. Vanhala, K. Palovuori, S. Tuukkanen, Adv. Funct. Mater. 24 (40) (2014) 6340–6347.
[314] S. Casaluci, M. Gemmi, V. Pellegrini, A. Di Carlo, F. Bonaccorso, Nanoscale 8 (9) (2016) 5368–5378.
[315] R.F. Hossain, I.G. Deaguero, T. Boland, A.B. Kaul, in: Proceedings of the 25th Biennial Lester Eastman Conference on High Performance Devices LEC 2016, 2016, pp. 19–22.
[316] Y. Yao, L. Tolentino, Z. Yang, X. Song, W. Zhang, Y. Chen, C.P. Wong, Adv. Funct. Mater. 23 (28) (2013) 3577–3583.
[317] Y. Xiao, L. Huang, Q. Zhang, S. Xu, Q. Chen, W. Shi, Appl. Phys. Lett. 107 (1) (2015) 013906.
[318] A.M. Joseph, B. Nagendra, E. Bhoje Gowd, K.P. Surendran, ACS Omega 1 (6) (2016) 1220–1228.
[319] D. Lee, S.H. Song, RSC Adv. 7 (13) (2017) 7831–7835.
[320] F. Torrisi, T. Carey, Printing 2D Materials, Flexible Carbon-based Electronics (eds P. Samorí and V. Palermo) (2018), http://dx.doi.org/10.1002/9783527804894.ch.

Tian Carey completed a honours bachelor degree in physics with astronomy and space science from University College Dublin in 2013 and subsequently completed an MPhil in Micro and Nanotechnology Enterprise in the University of Cambridge in 2014. He since joined the Department of Engineering at the University of Cambridge and completed his PhD in 2018 with Pembroke College, Cambridge. His research interests include printed and textile electronics, composites and energy harvesting with graphene and two-dimensional materials. He is currently working as an Enterprise Fellow of the Royal Academy of Engineering.

Felice Torrisi is a University Lecturer in graphene technology in the University of Cambridge and Fellow of Trinity College, Cambridge. He graduated at the University of Catania, Italy, after a research period at the Institute of Microelectronics and Microsystems of the Italian National Research Council. He joined the Department of Engineering at the University of Cambridge in October 2008 as PhD student, then as a Research Fellow and finally as a Lecturer in 2014. His research interests span from printed and flexible electronics to photonics with graphene and 2D materials, with particular focus on wearable and textile electronics.